

The evertng *Drosophila* wing disc is a shape-programmed material

Jana F. Fuhrmann^{1,2}, Abhijeet Krishna^{1,2,3}, Joris
Paijmans⁴, Charlie Duclut^{4,5}, Suzanne Eaton^{1,2,3,6}, Marko
Popovic^{2,3,4}, Frank Julicher^{2,3,4}, Carl D. Modes^{1,2,3*}
and Natalie A. Dye^{1,2,7*}

¹*Max-Planck Institute for Molecular Cell Biology and Genetics,
MPI-CBG, Pfotenhauerstrasse 108, Dresden, 01307, Germany.

²Excellence Cluster, Physics of Life, Technische Universität
Dresden, Arnoldstrasse 18, Dresden, 01307, Germany.

³Center for Systems Biology, Pfotenhauerstrasse 108, Dresden,
01307, Germany.

⁴Max-Planck Institute for Physics of Complex Systems,
MPI-PKS, Nöthnitzer Str. 38, Dresden, 01187, Germany.

⁵Laboratoire Physico-Chimie Curie, CNRS UMR 168, Institut
Curie, Université PSL, Sorbonne Université, Paris, 75005, France.

⁶Biotechnologisches Zentrum, Technische Universität Dresden,
Tatzberg 47-49, Dresden, 01307, Germany.

⁷Mildred Scheel Nachwuchszentrum P2, Medical Faculty,
Technische Universität Dresden, Dresden, 01307, Germany.

*Corresponding author(s). E-mail(s): modes@mpi-cbg.de;
natalie_anne.dye@tu-dresden.de;

Keywords: morphogenesis, *Drosophila*, wing disc, shape programming, cell
rearrangements, MyoVI

2 *The evertting Drosophila wing disc is a shape-programmed material*25

Abstract

26 How complex 3D tissue shape emerges during animal development remains an important open question in biology and biophysics.
27 Although it is well-established that tissue-scale patterns of in-plane cell behaviors can reshape a tissue in 2D, whether and how such patterns could also deform a tissue in 3D remains unclear. Meanwhile, recent advances in materials science, physics, and engineering have enhanced our ability to craft and understand inanimate "shape-programmable" materials capable of undergoing blueprinted 3D shape transformations arising from in-plane gradients of spontaneous strains. Here, we use this conceptual framework to understand eversion of the *Drosophila* wing disc, a complex 3D tissue reshaping event in wing development. Using quantification of spatial patterns of cell dynamics on an evolving 3D tissue surface, combined with physical modeling and genetic perturbation, we demonstrate that the wing can deform itself in 3D through large-scale patterning of in-plane cellular behaviors, primarily rearrangements. This work shows that concepts from shape-programming can be employed to understand animal tissue morphogenesis and suggests that there exist intricate patterns in nature that could present novel designs for shape-programmable materials.

46

Introduction

47 Epithelial tissues are sheets of tightly connected cells with apical-basal polarity that form the basic architecture of many animal organs. Deformations of animal epithelia in 3D can be mediated by external forces, either from neighboring tissue that induces buckling instabilities (e.g., [1–3]) or extracellular matrix that confines (e.g., [4]) or expands (e.g., [5]). Alternatively, local differences in mechanics at the apical and basal sides of the deforming epithelia itself can drive out-of-plane tissue shape changes (e.g., ventral furrow invagination in the *Drosophila* embryo (reviewed in [6]) and fold formation in *Drosophila* imaginal discs [7]).

56 Here, we describe a mechanism for generating complex 3D tissue shape involving tissue-scale patterning of in-plane deformations, analogous to the shape transformations of certain inanimate shape-programmable materials. These shape programmable materials experience *spontaneous strains*, where the local preferred lengths change in response to stimuli in a desired way. Globally patterned spontaneous strains can create a geometric incompatibility with the original shape, triggering a specific, desired 3D deformation ([8–10]). These ideas have already proved insightful to the understanding of differential growth mediated plant morphogenesis [11, 12]. Animal epithelia are more dynamic, however, able to change cell shape and size, as well as rearrange tissue topology. As these behaviours cause in-plane changes in local tissue dimensions, the ingredients for shape-programmability are, in principle, present.

To test these concepts in animal morphogenesis, we quantify tissue shape changes and cell behaviors in the *Drosophila* wing disc during a 3D morphogenetic process called eversion (Fig. 1a). Through eversion, the wing disc proper, an epithelial mono-layer, undergoes a shape deformation in which the future dorsal and ventral surfaces of the wing blade appose to form a bi-layer and escape the overlying squamous epithelium called the peripodial membrane. This process is triggered by a peak in circulating levels of the hormone 20-hydroxyecdysone (20E), analogous to an activator in shape-programming. This complex tissue shape change is independent of forces external to the wing disc, as demonstrated by its ability to occur in explant culture [13]. The shape changes of the disc proper also cannot be fully explained by removal of the peripodial membrane or extracellular matrix and appear to be self-sufficient, involving active cellular processes [14–18]. It has long been postulated that the eversion of wing (and leg) discs involves cell rearrangements and/or cell shape changes that resolve previously established morphological patterns [19–22]. Here, we test these hypotheses by systematic quantification and genetic perturbation of cell behaviors during eversion and demonstrate how cell behaviors contribute to tissue shaping using a physical model analogous to shape programming.

Although the mechanism presented here explains a specific morphogenetic process during *Drosophila* wing development, it has the potential to be a general mechanism of epithelial shaping. In addition, developing such a data-driven pipeline, exploiting both gradients in isotropic deformation as well as the anisotropic component of spontaneous strain, advances our ability to understand shape-programmable systems in general.

1 The wing pouch undergoes anisotropic curvature changes during eversion

We first sought to characterize the tissue shape changes happening during wing disc eversion. To this end, we explanted wing discs at fixed time intervals, from late larval stage (wL3) to 6 hours After Puparium Formation (hAPF). We imaged the wing discs using multi-angle light sheet microscopy and then reconstructed and analyzed the 3D image stack [23]. In this way, we capture the complex 3D shape changes happening throughout the wing disc during eversion (Fig. 1b, Supplementary Video 1). Focusing on the prospective wing blade region (so-called wing disc pouch), the most dramatic tissue shape changes can be seen in a central cross-section along the axis perpendicular to the dorsal ventral boundary (DVB), referred to as “across-DVB” (Fig. 1c,d, Extended Data Fig. S1b,c). We observe that the tissue becomes flatter as the dorsal and ventral surfaces appose, with curvature increasing at the DVB. In the perpendicular plane, taken through DVB (referred to as “along-DVB”), the tissue does not change as significantly, preserving curvature in this direction (Extended Data Fig. S1c-e, S5b,d). These data provide a quantitative view

4 The evertting *Drosophila* wing disc is a shape-programmed material

110 of the tissue shape changes taking place during eversion, demonstrating the
 111 development of strong shape anisotropy that is robust from wing to wing.

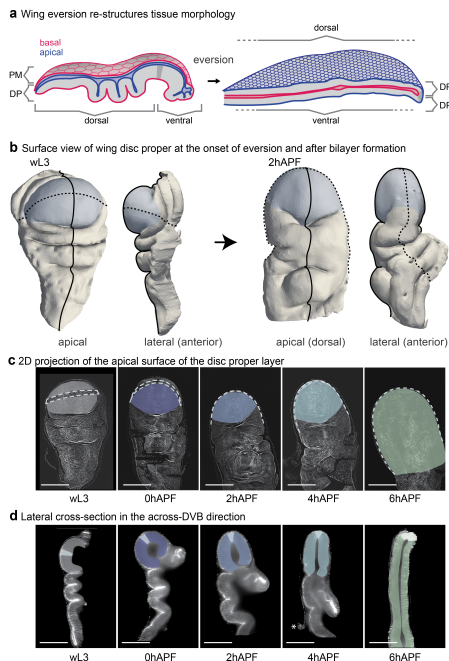


Fig. 1 **a**, Schematic cross-sections along the long axis of the wing disc before and after eversion. Before eversion, the wing disc resembles an epithelial sac with apical facing inwards. The tissue consists of the Disc Proper (DP), which is a folded, thick, pseudo-stratified monolayer, and the Peripodial Membrane (PM), a thin squamous monolayer. After eversion, the PM is removed and the former pouch region of the DP forms the wing bilayer with apical facing out and dorsal and ventral on opposing sides. **b**, Example of a 3D segmentation of the DP in a head-on and side view before eversion (left, wL3) and after bilayer formation (right, 2hAPF). Pouch: blue; across-DVB: solid line; along-DVB: dashed line. **c,d**, Representative images for stages of eversion. Wing discs are labelled with Ecadherin-GFP. The pouch region is highlighted, colored by time. **c**, Projection view showing the dorsal side for early pupal stages and dorsal (down), ventral (up), and DVB for wL3. The position of the DVB is indicated with a dashed line. **d**, Across-DVB cross-section. The position of the DVB is indicated in white. Asterisk shows the rupture point of the PM, which gets removed around 4hAPF. Minimum 5 wing discs were analyzed for each time point; hAPF = hours after puparium formation; wL3 = wandering larval stage, 3rd instar; scale bars = 100 μ m.

112 2 Programmable spring network as a model for 113 epithelial morphogenesis

114 We developed a coarse-grained model of tissue shape changes, leveraging an
 115 analogy between tissue remodelling by internal processes and spontaneous
 116 strain-driven shape programming of nematic elastomers [24–26]. We use a
 117 double layer of interconnected programmable springs representing the apical

surface geometry and the material properties of an epithelial sheet, including a 118
bending rigidity introduced by the thickness of the double layer (Methods 7.8, 119
7.13). As an initial configuration, we use a stress-free spherical cap and then 120
assign new rest lengths to the springs. In a continuum limit, this corresponds 121
to introducing a spontaneous strain field $\underline{\lambda}(\underline{X})$, which depends on the spatial 122
coordinates \underline{X} (Methods 7.9). To simplify notation, we write $\underline{\lambda}$ for $\underline{\lambda}(\underline{X})$ here- 123
after. To generate a final output shape, we quasi-statically relax the spring 124
network (Methods 7.8, 7.9). As with conventional elastic strain tensors, $\underline{\lambda}$ can 125
be decomposed into isotropic (λ) and anisotropic ($\tilde{\lambda}$) modes (Fig. 2a). 126

We first wanted to understand how simple choices of spontaneous strain 127
patterns induce a shape change in our model. A simple gradient of λ , for 128
example, causes the spherical cap to balloon in the center or generate wrinkles 129
at the periphery (Fig. 2b.i. and ii). Changing the directions and gradients of 130
 $\tilde{\lambda}$ leads to elongation of the cap, increase in the curvature at the tip or even 131
flattening of the curvature in the center, eventually leading to a saddle shape 132
(Fig. 2b.iii - viii.). 133

We propose that cell behaviors can give rise to a spontaneous strain field, 134
thereby shape-programming the wing disc pouch and driving 3D shape changes 135
during eversion. The spontaneous strains from these cell behaviors can be 136
represented in the programmable spring model by changes in the spring rest 137
lengths. We calculate a coarse-grained spontaneous strain from the underly- 138
ing cell behaviors, allowing us to leave the topology of the spring network 139
unchanged [27]. 140

We build our spontaneous strains from the strains that we infer from 141
observed cell behaviors during eversion, which we refer to as observed strains 142
 $\underline{\lambda}^*$. For the isotropic component, we focus on cell area changes (λ_A^*), as 143
cell division and cell death are minimal in the evertting wing disc (Fig. 2ci) 144
[13, 28, 29]. The anisotropic components of spontaneous strain capture contri- 145
butions stemming from both changes in cell elongation ($\tilde{\lambda}_Q^*$) as well as from 146
cell rearrangements ($\tilde{\lambda}_R^*$) (Fig. 2cii). 147

Our model can therefore relate cell behaviors to spontaneous strains in 148
order to understand resulting tissue deformations. We now investigate these 149
quantities in the evertting wing disc. 150

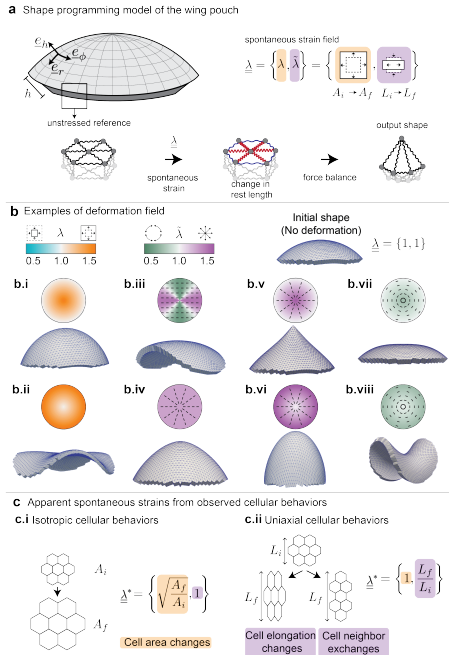
6 *The evertting Drosophila wing disc is a shape-programmed material*

Fig. 2 **a**, A thick spherical cap as a model for an epithelial tissue. We define a radial coordinate r and basis vectors e_r, e_ϕ , and e_h . The thickness of the spring network h is constant everywhere and introduces a bending rigidity. The model tissue is an elastic medium implemented as a spring network with an initially stress-free state. We change the rest lengths of the springs by imposing a spontaneous strain field $\underline{\lambda}$ and allow subsequent relaxation to take a new 3D output shape. Top and bottom springs at any position in the lattice have their rest lengths updated by the same amount. The spontaneous strain field $\underline{\lambda}$ consists of an isotropic component λ and an anisotropic component $\tilde{\lambda}$. These components cause changes in area (A_i to A_f) or area-preserving changes in shape (L_i to L_f), respectively. **b**, Model realizations with simple patterns of spontaneous strains. For each realization, the input pattern of spontaneous strains is displayed above, with the magnitude of strain encoded by color. For anisotropic strain ($\tilde{\lambda}$), the bars indicate the orientation. Below is the output shape. In **b.i-ii**, we vary the isotropic contribution λ and keep $\tilde{\lambda} = 1$, while in **b.iii-viii**, we vary $\tilde{\lambda}$ and keep $\lambda = 1$. We probe the model output from input linear radial gradients in λ or $\tilde{\lambda}$, giving rise to cones with varying degrees of sharpness at the tip (**i, v, vi, vii**) or saddle shapes (**ii, viii**). Using a spatially homogeneous pattern of $\tilde{\lambda}$, we observe an elongated spherical cap when patterned along a fixed direction (**iii**) and a blunt cone when patterned radially (**iv**). **c**, Schematics showing the calculation of apparent spontaneous strains from observed cellular behaviors. **c.i** For a patch of cells going from area of A_i to A_f , we extract λ . **c.ii** A patch of cells undergoing anisotropic deformation due to cell elongation changes or neighbor exchanges causes the length scale in one direction to change from L_i to L_f . From this change, $\tilde{\lambda}$ is extracted, while $\lambda = 1$, as there is no isotropic contribution.

151 **3 Spatial patterns of cell dynamics in the**
 152 **evertting wing pouch**

153 From larval stages, we know that cell behaviors in the pouch are organized
 154 radially in the region outside of the dorsal ventral boundary (outDVB) and

parallel to the boundary in the region closest to the dorsal ventral boundary (DVB) [30–33]. During eversion, we observe that cell shapes and sizes are patterned similarly. In early stages, cell area follows a radial gradient that disappears by the end of eversion (4hAPF) (Fig. 3a, Methods 7.6). Cell elongation exhibits a global nematic order through 4hAPF before disordering at 6hAPF (Fig. 3b, Methods 7.6).

To compare spatial patterns of cell behaviors over eversion time and across experiments, we define a coordinate system on the evolving 3D geometry. To this end, we use the cellular network topology to define the distance measure on the tissue surface. The topological distance between two cells is defined as the number of cells on the shortest path through the network from one cell to the other (See Extended Data Fig. S2a). We then use topological distance to define a coordinate system in the outDVB and DVB regions (Fig. 3c, Extended Data Fig. S2 and S3a,b, and Methods 7.7). The outDVB region consists of the dorsal and ventral halves, and we identify a single cell that defines the origin in each half (O_D and O_V). In the DVB, we define the origin (O_{DV}) as a line of cells transversing the DVB. The topological distance k to the origin defines a radial topological coordinate in each region, see Fig. 3c,d.

During eversion, the tissue unfolds and more of the pouch comes into view. In order to compare cell behaviors at different time points, we need to identify a region of tissue that remains in the field of view throughout eversion. To this end, we count the number of cells N_{ROI} within the largest visible topological ring at wL3. The corresponding region of interest at later time points is then defined to be centered at the origin and containing the same number of cells. Since there are very few divisions and extrusions during eversion [13, 28], and because cells cannot flow across the DVB [34, 35], we expect that our regions of interest contain largely the same set of cells, and we refer to them as topologically tracked regions (Fig. 3d,g, Extended Data Fig. S5a,b).

Next, we quantify patterns of cell area A and cell elongation as a function of topological coordinate k throughout eversion (See Methods 7.6). We find that our topological coordinate system recapitulates previously reported gradients in cell area and radial cell elongation at earlier larval stages (Extended Data Fig. S3c,d). In outDVB at wL3, we observe a cell area gradient that relaxes gradually until 4hAPF. At the same time, cell elongation develops a gradient, with cells in the periphery elongating tangentially (Fig. 3e,f). Between 4h and 6hAPF, cells dramatically expand their area and tangential cell elongation completely relaxes. We do not observe gradients in cell area or cell elongation in the DVB. Instead, cell area expands globally in the DVB during eversion, while cell elongation along the DVB first increases up to 2hAPF and then decreases at 4hAPF (Fig. 3e,f).

Using topological distance allows us to extract spatial patterns of oriented cell rearrangements from snapshots of eversion. Radially oriented rearrangements lead to a decrease in the number of cells per k , whereas tangentially oriented rearrangements lead to an increase (see Fig. 3g). As a consequence, $k(N_{ROI})$ changes based on the orientation and magnitude of rearrangements.

8 *The evertting Drosophila wing disc is a shape-programmed material*

200 We find that $k(N_{\text{ROI}})$ increases with time (Fig. 3g), consistent with radially
201 oriented cell rearrangements in outDVB and rearrangements oriented along
202 the boundary in the DVB.

203 Together, these measured cell behaviors are a superposition of different
204 radial patterns with the additional complexity of the DVB. Next, using our
205 programmable spring model (Fig. 2), we asked how in-plane strains caused by
206 these cell behaviors could drive 3D shape changes during eversion.

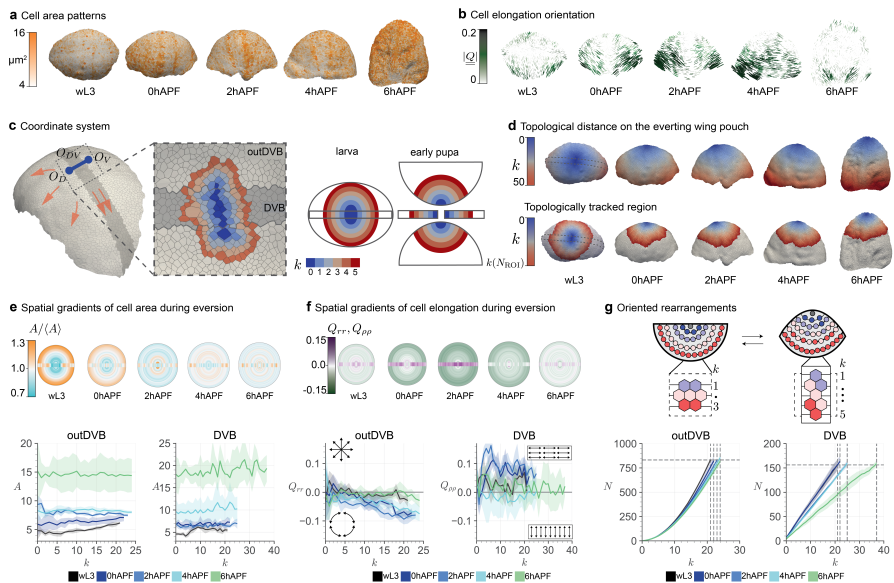


Fig. 3 a,b,d, Cell measurements highlighted on the surface of representative examples of evertng wing discs over time. At wL3, the full pouch is visible, whereas only the dorsal side is shown here for early pupal stages. **a**, Cells are colored by apical cell area. **b**, Bars highlight the orientation of locally averaged cell elongation Q (projected onto 2D), and color indicates the elongation magnitude $|Q|$ averaged over patches of size $350\mu\text{m}^2$. **c**, Segmentation of a wL3 pouch; the origins for the topological coordinates k (O_D and O_V in the outDVB region and a center line O_{DV} for the DVB) are highlighted in dark blue. The arrows indicate the direction of spatial coordinates that result from these origins, transversing along the DVB and radially for the outDVB. The inset shows the center region of the same wing pouch, where each cell up to $k = 5$ is colored by k . The origin cells are at $k = 0$ (dark blue). Note that the origin is a single cell for each side of the outDVB and a line of cells for the DVB. Due to the 3D nature of the wing pouch, the topological coordinate system is defined in one view for larval stages and in 4 separate imaging angles for early pupal stages (see schematic, right). **d**, The maximum k depends on the size of the segmented region (upper row). For the topologically tracked region, the maximum k may change due to rearrangements and is denoted $k(N_{ROI})$ (lower row). **e-f**, Cell area (e) or cell elongation (f) spatially averaged over k (minimum five wing discs per stage). Dorsal and ventral are averaged together into 'outDVB'. Geometric representations (top) show outDVB as half-circles and the DVB as a central rectangular box. **e**, Geometric representations highlight cell area gradients ($A/\langle A \rangle$) within each stage. Lower panels show the cell area (A) as a function of k for all time points. **f**, The component of cell elongation (Q_{rr} for cells in the outDVB and $Q_{\rho\rho}$ for cells in the DVB) is calculated relative to the origin for each cell of the respective region. This makes Q_{rr} the radial component of cell elongation, whereas $Q_{\rho\rho}$ is effectively the cell elongation along the DVB (cartoon insets on the lower panel, see also Methods 7.7). Q_{rr} and $Q_{\rho\rho}$ are calculated as a function of k . In the upper panel, magnitudes are represented by color. **g**, Schematic (top) showing how we estimate cell rearrangements using topology. Each circle represents a cell in the outDVB region of the wing disc, colored by topological distance at the initial time point. If the number of cells per k decreases, the deformation by rearrangements is radial. Plots (bottom) show the number of cells in the wing disc pouch N contained within k . The horizontal line shows N_{ROI} for the wL3 stage; the vertical lines show corresponding ($k(N_{ROI})$) for each stage. In **e-g**, solid lines indicate the mean, and ribbons show 95% confidence of the mean.

207 **4 Cell rearrangements drive wing pouch**
 208 **eversion**

209 To compare the output of the model to the 3D shape changes happening during
 210 eversion, we quantified the curvature and size dynamics of the apical surface of
 211 the wing pouch. We limit the analysis to the topologically tracked region and
 212 quantify the change in curvature from the wL3 stage along lines in the along-
 213 DVB and across-DVB directions (Fig. 1b-d, Extended Data Fig. S5, Methods
 214 7.12). We focus on the stages between wL3 and 4hAPF, during which cell shape
 215 patterns have radial symmetry (Fig. 3b,e,f). We observe an overall curvature
 216 increase that is more pronounced in the across-DVB direction, peaking at the
 217 DVB, while flattening at the dorsal and ventral sides. Furthermore, the overall
 218 tissue area increases (Fig. 4a, Extended Data Fig. S5a).

219 Next, we measure the strain field ($\underline{\lambda}^*$, Fig. 4b) resulting from cell behaviors
 220 as a function of the distance from the origin, r or ρ (Fig. 4b, Extended Data
 221 Fig. S6, Extended Data Fig. S7, Methods 7.11). We quantify the isotropic
 222 component resulting from cell area changes (λ_A^*). In the outDVB, we observe an
 223 area expansion ($\lambda_A^* > 1$) up to 2hAPF with a radially decreasing profile (Fig.
 224 4b, Extended Data Fig. S7). In the DVB, we observe the buildup of a shallower
 225 gradient that is transiently paused from 0hAPF to 2hAPF. The contribution
 226 to the anisotropic component of $\underline{\lambda}^*$ from changes in cell elongations $\tilde{\lambda}_Q^*$ is
 227 small compared to the contribution by cell rearrangements $\tilde{\lambda}_R^*$. While $\tilde{\lambda}_Q^*$ is
 228 tangential, following a shallow gradient, $\tilde{\lambda}_R^*$ is radial and increasing with the
 229 distance from origin in the outDVB and decreasing in the DVB (Fig. 4b,
 230 Extended Data Fig. S7, Methods 7.10).

231 We next use the programmable spring model to test how the observed in-
 232 plane cellular behaviors can cause tissue shape changes. We define the DVB
 233 and outDVB regions in the model, matching their relative sizes in the wing
 234 pouch (Fig. 4c, Extended Data Fig. S8). For each individual cell behavior and
 235 measured time point (wL3, 0hAPF, 2hAPF, and 4hAPF), we use the in-plane
 236 strain $\underline{\lambda}^*$ that we infer from each observed class of cell behaviors as examples
 237 of spontaneous strain $\underline{\lambda}$. We use these to program the spring lengths in the
 238 model. For each insertion of spontaneous strain (model time points: initial,
 239 t1, t2, final, corresponding to the experimental time points), we relax the
 240 spring network quasi-statically to a force balanced state (Methods 7.8, 7.9). As
 241 the effective bending modulus of the wing disc is experimentally inaccessible,
 242 we fit the thickness of the model in an example scenario where all observed
 243 cell behaviours are input as spontaneous strains and use the same thickness
 244 thereafter (Extended Data Fig. S9a, Methods 7.13).

245 We first consider cell rearrangements as a possible source of spontaneous
 246 strain. When we only input $\underline{\lambda}_R = \{1, \tilde{\lambda}_R^*\}$ as spontaneous strain in the model,
 247 it alone creates a strong curvature increase, resembling many features of the
 248 data but without increasing tissue size (Fig. 4a, d). Note that $\underline{\lambda}_R$ also breaks
 249 the symmetry between the two directions, across-DVB and along-DVB, at the
 250 final stage.

After relaxing the spring network to a force balanced state, stresses due to residual strains remain. The stresses corresponding to these residual strains can drive passive responses in cell behaviors. The residual strains appear as a mismatch of spontaneous strains (input to the model, $\underline{\lambda}$) and strains resulting from changes in spring length during relaxation of the network, \underline{F} (Fig. 4e.i, Methods 7.9). 251
252
253
254
255
256

When we calculate the residual strains generated by spontaneous strain from rearrangements, we find that the anisotropic component of the residual strain ($\tilde{\lambda}_R^{\text{res}}$) is tangentially oriented (Fig. 4e.ii, Extended Data Fig. S10). This tangentially oriented strain is similar to the pattern of cell elongation changes ($\tilde{\lambda}_Q^*$) (compare Fig. 4b and 4e.ii), suggesting that these cell elongation changes are a passive response to spontaneous strain by rearrangements. To test this idea, we next consider cell elongation as possible source of spontaneous strain. When we only input $\underline{\lambda}_Q = \{1, \tilde{\lambda}_Q^*\}$ as spontaneous strain in the model, we observe that the spring network shape flattens at the center rather than curve, and cell elongations themselves do not lead to any further residual strains (Fig. 4f,g, Extended Data Fig. S10). This result is consistent with cell elongation changes being a passive response to cell rearrangements and not driving tissue shape change during eversion. 257
258
259
260
261
262
263
264
265
266
267
268
269

Cell rearrangements as spontaneous strains also lead to residual isotropic compression (λ_R^{res} , Fig. 4e.ii, Extended Data Fig. S10). This residual could be compensated by spontaneous area change, which is also required by the observation that overall tissue size increases during eversion. 270
271
272
273

When we only input the isotropic strain, $\underline{\lambda}_A = \{\lambda_A^*, 1\}$, from observed cell area changes as spontaneous strain in the model, overall size increases with minimal curvature change (Fig. 4h). This result indicates that although cell area changes are an active behavior and lead to overall size increase, they do not significantly contribute to changes in tissue shape. However, there does appear to be a transient effect of cell area changes on tissue curvature at time point t2. This transient effect in the scenario of spontaneous area strain only arises from the experimentally observed pause in cell area expansion in the DVB at 2hAPF as compared to the outDVB (Extended Data Fig. S7). It later disappears in the model when the cell area in the DVB expands to match the outDVB at 4hAPF (Fig. 4e). Measuring $\underline{\lambda}_A^{\text{res}}$, we find that cell area changes themselves create a small residual in the DVB (Fig. 4i, Extended Data Fig. S10). The anisotropic part of this residual could also contribute to the observed passive cell elongations. 274
275
276
277
278
279
280
281
282
283
284
285
286
287

Using these examples, we next infer the spontaneous strain patterns that drive tissue shape changes and govern cellular behaviors. We have found that both cell rearrangements and cell area changes are active and contribute to spontaneous strain. We therefore conclude that cell elongation is a passive elastic response and does not contribute to spontaneous strain. The total spontaneous strain, therefore, is composed of the anisotropic part of the observed strain due to rearrangements ($\tilde{\lambda}_R^*$, Fig. 4b) and the isotropic part of the 288
289
290
291
292
293
294

12 *The evertng Drosophila wing disc is a shape-programmed material*

295 observed cell area changes (λ_A^*) compensated by the isotropic part of the resid-
296 ual strain due to cell rearrangements (λ_R^{res} , Fig. 4e.ii). Fig. 4j shows the shape
297 changes generated by this total spontaneous strain, which accounts for the cur-
298 vature and size changes observed from wL3 to 4hAPF in the evertng wing disc
299 (see also Extended Data Fig. S9b). The good qualitative agreement between
300 model output and wing pouch curvature changes indicates that we have iden-
301 tified the most relevant active cellular events responsible for the pouch shape
302 change during eversion. Furthermore, the patterns of residual strains gener-
303 ated by the model provide a prediction of the mechanical stresses present in
304 the wing disc pouch after eversion. In particular, after eversion (at 4hAPF),
305 cells experience elongation due to shear stress as well as area constriction due
306 to compressive stresses (Fig. 4k, Extended Data Fig. S7).

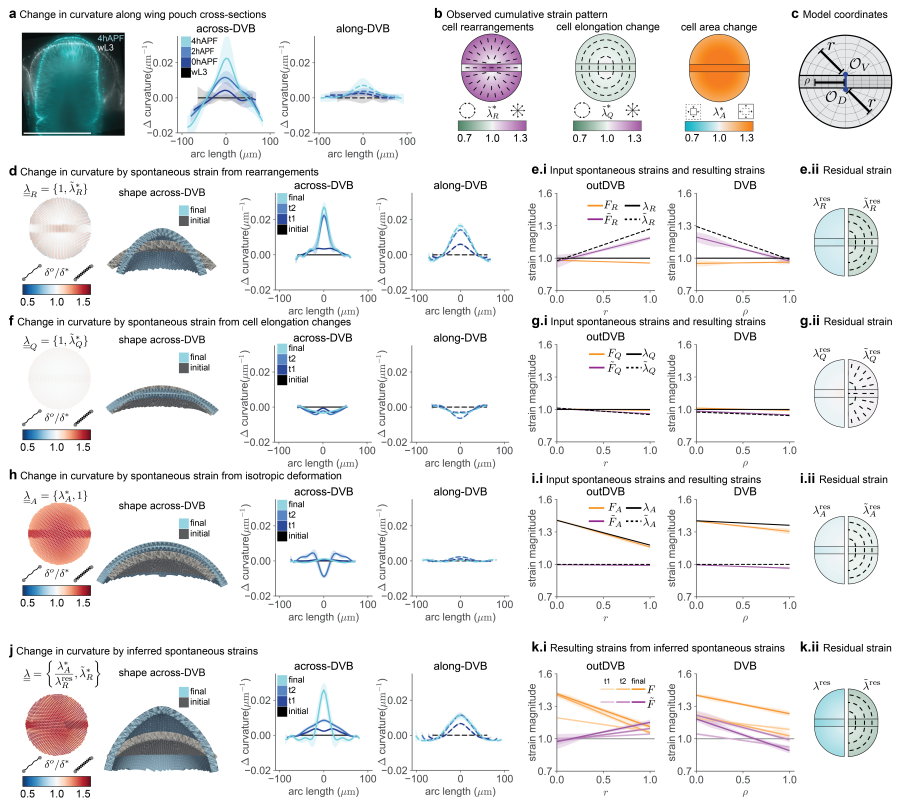


Fig. 4 **a**, Overlay of a wL3 (white) and a 4hAPF (cyan) wing pouch (left) and plots of the average change in tissue curvature in the topologically tracked region in across-DVB (middle) and along-DVB (right) directions. **b**, Observed strain from cellular behaviors between time points wL3 to 4hAPF as a function of normalized distance from origin r and ρ . Observed strains arise from (left to right): rearrangements ($\tilde{\lambda}_R^*$), cell elongation changes ($\tilde{\lambda}_Q^*$), and cell area changes (λ_A^*). Half circles indicate the outDVB region; the rectangular box indicates the DVB. The color represents the magnitude of different strains; the bars visualize the direction of observed strain for $\tilde{\lambda}_R^*$ and $\tilde{\lambda}_Q^*$. **c**, The model coordinates are designed to match the geometry of spatial patterns in the wing disc pouch (See also Fig. 3c). **d,f,h** Observed in-plane strain from rearrangements (**d**, $\tilde{\lambda}_R^*$), cell elongation changes (**f**, $\tilde{\lambda}_Q^*$), and cell area changes (**h**, λ_A^*) are inserted in the model as spontaneous strains by a change in rest length of the springs (δ^o/δ^*). To compare the initial and final stages (corresponding to wL3 to 4hAPF), the model cross-section shows the shape in the across-DVB direction. The change in curvature of the model outcomes are plotted for all time points (right) in the across-DVB and along-DVB directions. The initial shape is a spherical cap with a radius resembling the wL3 stage. t1,t2, and final stages are the model results from the change in strains by 0,2, and 4hAPF. $\underline{\lambda}$ contains observed strains from the individual measured cell behaviors, while the other components (λ or $\tilde{\lambda}$) are set to 1. **e.i,g.i,i.i**, Input spontaneous strain for $\tilde{\lambda}_R^*$ (**e**), $\tilde{\lambda}_Q^*$ (**g**), and λ_A^* (**i**) at the final eversion time point (λ , $\tilde{\lambda}$) and the resulting strain that is achieved after relaxation of the model, which can be isotropic (F) and anisotropic (\tilde{F}). **e.ii,g.ii,i.ii**, Residual strain that remains at the final time point. The colors shows the magnitude of strain using the same range as indicated in Fig. 4b. Plots are split vertically to show the isotropic component (λ) on the left and the anisotropic component ($\tilde{\lambda}$) on the right. **j, k**, Model output and residual strains for the inferred spontaneous strains, following the same procedure as in **d-i**.

307 **5 MyoVI knockdown alters active cell behaviors**
 308 **resulting in a tissue shape phenotype**

309 So far, our analysis has revealed that active in-plane cell behaviors can drive
 310 tissue shape changes in the wing blade during eversion. We now use a genetic
 311 perturbation to confirm the role of active cell behaviors. Previous work in
 312 the wing disc pouch of earlier larval stages showed that cell rearrangements
 313 drive cell shape patterns [33]. This work suggested that patterns of active
 314 cell rearrangements self-organize via mechanosensitive feedback mediated by
 315 MyoVI. We therefore next investigate whether MyoVI knockdown in the wing
 316 pouch (Extended Data Fig. S11) alters cell rearrangements during eversion
 317 and leads to a tissue shape phenotype.

318 We observe that the MyoVI^{RNAi} wing disc fails to form a flat bi-layer
 319 after eversion, even though its initial shape is similar to the *wild type* (wt)
 320 (Fig. 5a.i). This phenotype is best captured in the behavior of curvature in
 321 the across-DVB direction (Fig. 5a.ii). Here, the curvature decreases in the
 322 center, in contrast to wt, where it increases. In the along-DVB direction, the
 323 curvature remains unchanged over time in the MyoVI^{RNAi} knockdown (Fig.
 324 5a,b, Extended Data Fig. S11c-d). Other features of eversion, such as the
 325 opening of the folds and the removal of the peripodial membrane are unaffected
 326 by the MyoVI^{RNAi} knockdown (Fig. 5a, see 4hAPF), indicating that the cause
 327 for the altered shape is pouch-intrinsic. This result further supports the idea
 328 that tissue shape changes in the wing pouch during eversion are independent
 329 of other morphogenetic events.

330 Next, we quantified cell behaviors in MyoVI^{RNAi}. While initially the gradi-
 331 ents in cell areas and elongation are similar to wt (Extended Data Fig. S11e,f),
 332 the inferred strains from individual types of cell behaviors $\underline{\lambda}^*$ differ (Fig. 5c,
 333 Extended Data Fig. S12). From work in earlier larval stages, we expect oriented
 334 rearrangements to be reduced [33]. Indeed, we find that MyoVI^{RNAi} reduces
 335 the amount of radial cell rearrangements in the outDVB during eversion. How-
 336 ever, in the DVB, rearrangements are of opposite orientation as compared to
 337 wt eversion. Notably, we also see a complete lack of cell area expansion in the
 338 DVB. The pattern of cell elongations in the outDVB is similar to wt, but in
 339 the DVB it is of perpendicular orientation.

340 Using the programmable spring model, we test how the reduction of spon-
 341 taneous strain due to cell rearrangements affects tissue shape changes. When
 342 we input $\underline{\lambda}_R = \{1, \tilde{\lambda}_R^*\}$ from cell rearrangements measured in MyoVI^{RNAi} as
 343 spontaneous strain in the model, we see only a slight increase in curvature
 344 in the final time point in both along- and across-DVB directions (Fig. 5d).
 345 Thus, we conclude that the reduction of cell rearrangements in MyoVI^{RNAi} as
 346 compared to wt contributes to the abnormal tissue shape changes happening
 347 during eversion in MyoVI^{RNAi}. We find that the anisotropic component of the
 348 residual strain (λ_R^{res}) is small and tangentially oriented in the outDVB and
 349 radially in the DVB, similar to the cell elongation pattern (Fig. 5c,e, Extended
 350 Data Fig. S13). If we input measured cell elongation changes as spontaneous

strain in the model ($\underline{\lambda}_Q = \{1, \lambda_Q^*\}$), we do not recapitulate the observed tissue shape changes (Extended Data Fig. S14). This result suggests that the cell elongation changes in MyoVI^{RNAi} are a passive response to spontaneous strain by cell rearrangements, as in wt.

While the change in spontaneous strain due to rearrangements captures a significant portion of the difference between the wt and MyoVI^{RNAi}, it fails to recapitulate the finer progression of shape from wL3 to 4hAPF in MyoVI^{RNAi}. In particular, the curvature at the final time point of the model calculation is not flattened in the center of the across-DVB direction, and the curvature increases slightly in both directions (Fig. 5b,d).

Thus, we proceed to input the observed cell area changes as spontaneous strains in the model ($\underline{\lambda}_A = \{\lambda_A^*, 1\}$). We find that they produce shape changes over time similar to those observed during MyoVI^{RNAi} eversion, recapitulating both the decrease in curvature in the center of the across-DVB direction and the lack of curvature change in the along-DVB direction (Fig. 5f). We conclude, therefore, that the subtle flattening in the pouch center in MyoVI^{RNAi} during eversion can be explained by the combination of cell area expansion in the outDVB with no area expansion in the DVB. This result highlights that, while cell area changes do not lead to a curvature change in wt, the difference in area expansion between the tissue regions results in the MyoVI^{RNAi} shape. In addition, although we did not observe cell area expansion in the DVB, the area expansion in the outDVB creates residual strains in both regions (Fig. 5g, Extended Data Fig. S13). These residual strains have an anisotropic component that, together with the residual strains from cell rearrangements, account for the measured cell elongation patterns in MyoVI^{RNAi} (compare Fig. 5c,e.ii,g.ii)).

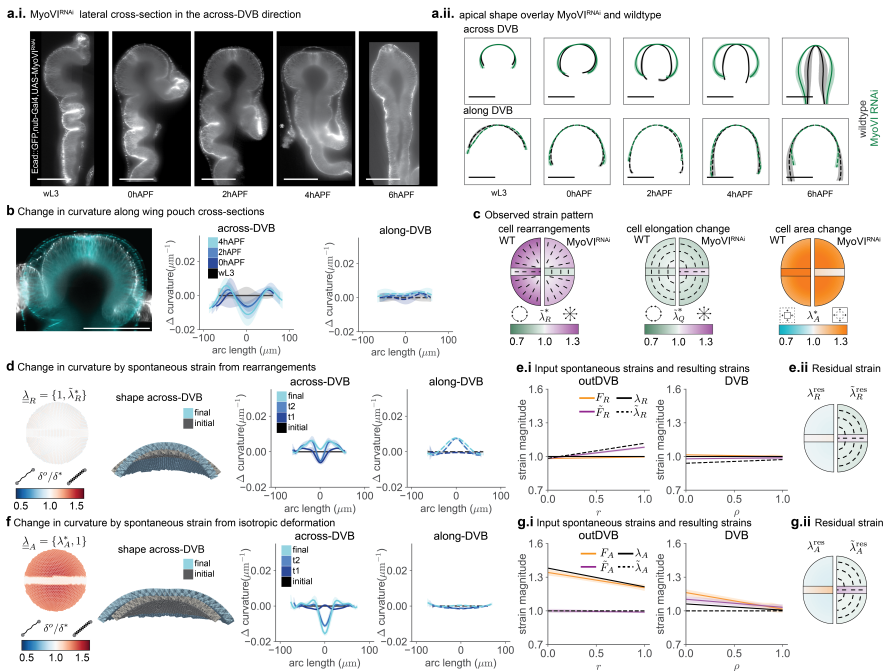
16 *The evertng Drosophila wing disc is a shape-programmed material*

Fig. 5 **a**, MyoVI^{RNAi} phenotype during eversion (scale bars = 100 μm). Representative across-DVB cross-sections (**a.i**) and comparison of apical shape between MyoVI^{RNAi} and control (**a.ii**). **b**, Overlay of a wL3 (white) and a 4hAPF (cyan) MyoVI^{RNAi} wing pouch (left) and plots of the average change in tissue curvature in the topologically tracked region for across-DVB (middle) and along-DVB (right) directions. **c**, Observed strain from cellular behaviors in MyoVI^{RNAi} wing discs between time points wL3 to 4hAPF. Plots are split vertically with the observed strains for *wild type* (WT) for comparison on the left and MyoVI^{RNAi} on the right. Measured strains come from λ_R^* , λ_Q^* , and λ_A^* . Quarter circles indicate the outDVB region, and the rectangular box indicates the DVB. The color represents the magnitude of different strains; the bars indicate the direction of observed strain for λ_R^* and λ_Q^* . **d,f**, Observed in-plane behaviors are inserted in the model as spontaneous strains by a change in rest lengths of the springs (δ°/δ^*). The initial stage is a spherical cap with the radius taken to resemble the shape at the *wild type* wL3 stage. t1,t2, and final stages are the model results after a change in spring rest length according to observed strains from 0,2, and 4hAPF for MyoVI^{RNAi}. $\underline{\lambda}$ contains observed strains from rearrangements (**d**) or area changes (**f**), while the other components (λ_R or λ_A) are set to 1. **e.i,g.i**, Input spontaneous strain ($(\lambda$ and $\tilde{\lambda}$) at the final eversion time point and comparison with the resulting strain that is achieved after relaxation of the model (F and \tilde{F}). **e.ii,g.ii**, Residual strain that remains from the difference between input and resulting spontaneous strain at the final time point, plotted in the same way as Fig. 4e,g,i,k.ii.

377 **6 Discussion**

378 In this work, we show that 3D epithelial tissue morphogenesis in the *Drosophila*
 379 wing disc is based on in-plane spontaneous strains generated by active cellular
 380 behaviors. We develop a metric-free, topological method to quantify patterns
 381 of cell dynamics on arbitrarily shaped tissue surfaces, as well as a theoretical

The evertng Drosophila wing disc is a shape-programmed material 17

approach to tissue morphogenesis inspired by shape-programmable materials. 382
 These advancements together reveal the mechanics of tissue shape changes 383
 during wing disc eversion, showing that active rearrangements and active area 384
 expansion govern the 3D tissue shape and size changes. 385

We hypothesize that the organization of active behaviors during wing ever- 386
 sion arises from patterning during larval growth. First, the pre-patterned radial 387
 cell area gradient resolves during eversion, giving rise to a gradient of spon- 388
 taneous strain in the outDVB. Second, the orientation of cell rearrangements 389
 follows that of earlier stages, indicating that the mechanosensitive feedback 390
 that was revealed in previous work is still active during eversion. Overall, this 391
 suggests a developmental mechanism through which mechanical cues at early 392
 stages organize cell behavior patterns that later resolve, resulting in a shape 393
 change. Such behavior would resemble biochemical pre-patterning, in which 394
 cell fates are often defined long before differentiation. 395

Active, patterned rearrangements can robustly give rise to a specific target 396
 shape if the tissue is solid on the time scale of morphogenesis. Our work there- 397
 fore reveals that the evertng wing disc behaves as an elastic solid undergoing 398
 plastic deformation and demonstrates that the mere presence of rearrange- 399
 ments should not be taken as a sign of a fluid tissue with a vanishing elastic 400
 modulus. Many animal tissues with dynamic rearrangements could thus be in 401
 the solid regime and therefore be pre-patterned towards a target shape. Our 402
 work, inspired by shape programmability of complex materials, reveals prin- 403
 ciples of shape generation that could be quite general. We therefore propose 404
 that many other morphogenetic events could and should be considered – and 405
 better understood – through the lens of shape-programmability. 406

7 Methods

7.1 Experimental model

All experiments were performed with publicly available *Drosophila* 409
melanogaster lines. Flies were maintained at 25°C under 12hr light/dark cycle 410
 and fed with standard food containing cornmeal, yeast extract, soy flour, malt, 411
 agar, methyl 4-hydroxybenzoate, sugar beet syrup, and propionic acid. Adult 412
 flies were transferred to fresh food 2-3 times per week. Only males were stud- 413
 ied for consistency and due to their smaller size. As *wild type*, we used the F1 414
 offspring of a cross between *w;-ecad::GFP* and *w;nub-Gal4,ecad::GFP;;*. 415

7.2 *Drosophila melanogaster* lines

genotype	construct	origin
<i>w;-; ecad::GFP;;</i>	Ecadherin::GFP	Bloomington #60584
<i>w; nub-Gal4, ecad::GFP;;</i>	nub-Gal4	Bloomington #86108
<i>w;-; ecad::GFP, myoVI^{RNAi};;</i>	MyoVI ^{RNAi}	VDRC #37534

417 7.3 Image acquisition and processing

418 **Sample preparation:** Wing discs of larval stages were dissected in culture
419 medium as previously described [36], without surface sterilization or antibiotics.
420 Prepupal stages from 0 to 6 hAPF required a slightly different dissection
421 strategy. Prepupae were marked by the time of white Pupa formation and
422 collected with a wet brush after the required time interval. Next, pupae were
423 placed on a wet tissue, cleaned with a wet brush to remove residual food,
424 and transferred into glass staining blocks (see Ref. [36]) filled with dissection
425 medium. To dissect the wing disc, a small cut was performed with fine surgical
426 scissors (2.5 mm, FST 15000-08, Fine Science Tools GmbH) at the posterior
427 end, which creates a small hole to release pressure. This allowed for the next
428 cut to be performed at half the anterior-posterior length, separating the ante-
429 rior and posterior halves. Next, the anterior part of the puparium was first
430 opened at the anterior end by administering a cut just posterior to the spiracles
431 and then a second cut was performed on the ventral side along the PD-axis.
432 The pupal case was then held open with one forceps, and a second forceps in
433 the other hand was used to remove the wing disc . To dissect wing discs from
434 0hAPF, the pupa is still soft enough to be turned inside-out after the cut that
435 separates anterior and posterior halves, similar to larval stages.

436 **Imaging:** Imaging was performed with a Zeiss Lightsheet 1 system. Wing
437 discs were mounted in capillaries (Zeiss, Capillary size 1, inner diameter ca.
438 0.68 mm) with 1 % low melting-point agarose (LMA, Serva, CAS 9012-36-6).
439 LMA was prepared by mixing 1:1 of Grace's insect medium and a 2% LMA
440 stock solution in water. Wing discs were transferred into mounting medium in
441 U-glass dishes, aspirated into the capillary at room temperature, and imaged
442 immediately after the LMA solidified. The imaging chamber was filled with
443 Grace's insect medium (measured refractive index = 1.3424). For pupal stages,
444 four imaging angles (dorsal, ventral, and 2 lateral) with 90° rotation were
445 acquired; for larval stages, three imaging angles (dorsal and ventral in one,
446 and 2 lateral) were acquired. Data from dual illumination was fused on the
447 microscope using a mean fusion.

448 **Multiview reconstruction:** Multiview reconstruction was based on the
449 BigStitcher plugin in Fiji [23, 37]. Images were acquired without fluores-
450 cent beads, and multiview reconstruction was done using a semi-automated
451 approach. Individual views are manually pre-aligned. Thereafter, precise mul-
452 tiview alignment was computed based on bright spots in the data with an
453 affine transformation model using the iterative Closest Point (ICP) algorithm.
454 Next, images were oriented to show the apical side in XY and lateral in ZY.
455 Lastly, images were deconvolved using point spread functions extracted from
456 the bright spots and saved as tif files with a manually specified bounding box.

457 **Surface extraction of 3D images for visualization:** Surfaces shown in
458 Fig. 1 and Supplemental movies were extracted from 2hAPF and wL3 images.
459 To do so, we first trained a pixel classifier on the strong apical signal of
460 Ecadherin-GFP of a different image of the same stage with napari-accelerated-
461 pixel-and-object-classification [38, 39]. Feature sizes of 1-5 pixels were used to

predict the foreground on the target image. Next, we used the pyclesperanto library [40] to select the largest labels and close gaps in the segmentation with the closing sphere algorithm. For additional gap-filling in the 2hAPF time point, we used vedo [41] to generate a pointcloud and extract the pointcloud density. When necessary, we applied some manual pruning of the segmentation in napari. We repeated this processing on the weak Ecadherin-GFP signal from the lateral membrane and subtracted the apical segmentation from the output. As a result, we achieve a full tissue segmentation that stops just below the apical junction layer. We then extracted the surface by the napari-process-points-and-surfaces [42] library and applied smoothing and filling holes. The visualizations were generated using Paraview [43]. Regions and directions of the cross-sections were annotated in Illustrator. Supplemental movies were created using paraview and Fiji [37].

7.4 Segmentation of the apical junction network

 475

To analyze cell shapes, we use four angles separated by 90° for the segmentation of early pupal stages, and a single angle for larval wing discs (Extended Data Fig. S4). Z-stacks from each imaging angle were denoised if necessary, by using the N2V algorithm [44], and the signal to background ratio was further improved by background subtraction tools in Fiji [37]. We made 2D projections of the Ecadherin-GFP signal in the Disc Proper layer as previously described [45]. Importantly, this algorithm also outputs a height-map image, which encodes the 3D information in the intensity of each pixel. The cells in the wing pouch were segmented using Tissue Analyzer and manually corrected [46]. We chose a bond length cutoff of 2 pixels ($\sim 0.46\mu\text{m}$). The ventral side for 0 hAPF was excluded from the analysis, as at this stage, the ventral region is never fully in view from any imaging angle. The number of wing discs per time point and the images for each region are indicated in Table 1. Images were rotated to orient distal down. Height-map images were rotated accordingly using imagemagickTM software (ImageMagick Development Team, 2021). We use Fiji macros included with TissueMiner [47] to manually specify regions of interest (ROIs). The DV boundary is identified based on Ecadherin-GFP signal intensity [48] and the dorsal vs. ventral pouch by their positions relative to global tissue morphology. For larval stages, the DV boundary, dorsal, and ventral regions are identified in one image. For images showing lateral views of pupal stages, the DV boundary is identified, whereas for images showing the outDVB region, the dorsal or ventral region and the cells next to the DV boundary are labelled. The cells next to the DV boundary are required as a landmark for topological analysis but are otherwise not analysed separately. We then run the TissueMiner workflow to create a relational database.

Table 1 wing disc data

Genotype	Stage	Number of wing discs	ROI	Replicates
E-cad::GFP, nub-Gal4	96hAEL	7	DVB	7
			dorsal	7
			ventral	7
	120hAEL	5	DVB	5
			dorsal	5
			ventral	5
		wL3	DVB	5
			dorsal	5
			ventral	5
			DVB	7
			dorsal	7
			DVB	5
			dorsal	5
			ventral	5
		0hAPF	DVB	7
			dorsal	7
			DVB	7
			dorsal	7
			ventral	7
			DVB	7
			dorsal	7
			DVB	6
			dorsal	4
			ventral	4
			DVB	5
E-cad::GFP, nub-Gal4, MyoVIRNAi	wL3	5	dorsal	5
			ventral	5
	0hAPF	DVB	6	
		dorsal	6	
		DVB	6	
		dorsal	5	
		ventral	6	
		DVB	5	
		dorsal	5	
		ventral	5	
		DVB	7	
		dorsal	6	
		ventral	6	

501 7.5 3D cellular network

502 We represent the configuration of the cellular network by positions of the cell
 503 vertices, where three or more cell bonds meet, and their topological relations
 504 as in TissueMiner [47]. We extend TissueMiner to the third dimension using
 505 the information extracted from height-maps, as described in Methods 7.4.

506 7.6 Measurement of cell area and cell elongation tensor

507 Each cell α in the 3D network contains N^α vertices \underline{v}_i^α , defining the network
 508 geometry. For every cell, we define a centroid \underline{R}^α , an area A^α , and a unit
 509 normal vector $\hat{\underline{N}}^\alpha$ as

$$\underline{R}^\alpha = \frac{1}{N^\alpha} \sum_{i=1}^{N^\alpha} \underline{v}_i, \quad A^\alpha = \frac{1}{2} \sum_{i=1}^{N^\alpha} \|\underline{n}_i^\alpha\|, \quad \hat{\underline{N}}^\alpha = \frac{1}{\|\sum_{i=1}^{N^\alpha} \underline{n}_i^\alpha\|} \sum_{i=1}^{N^\alpha} \underline{n}_i^\alpha \quad (1)$$

where $\underline{n}_i^\alpha = (\underline{v}_{i+1}^\alpha - \underline{v}_i^\alpha) \times (\underline{R}^\alpha - \underline{v}_i^\alpha)$ is the normal vector on the triangle formed by one edge of the cell and the vector pointing from the cell vertex to the cell centroid. It has a norm equal to twice the area of the triangle.

We then create a subcellular triangulation by connecting the two consecutive vertices in every cell with its centroid $\{\underline{v}_i, \underline{v}_{i+1}, \underline{R}^\alpha\}$. This creates a complete triangulation that depends both on the vertex positions and the centroids of the cellular network.

Each triangle is defined by its three vertices $\{\underline{R}_0, \underline{R}_1, \underline{R}_2\}$, which define two triangle vectors $\underline{E}_1, \underline{E}_2$ and its unit normal vector $\hat{\underline{N}}$

$$\underline{E}_1 = \underline{R}_1 - \underline{R}_0, \quad \underline{E}_2 = \underline{R}_2 - \underline{R}_0, \quad \hat{\underline{N}} = \frac{\underline{E}_1 \times \underline{E}_2}{\|\underline{E}_1 \times \underline{E}_2\|}. \quad (2)$$

These vectors also define the local basis on the triangle. Using the triangle vectors, we can define the area of the triangle and the rotation angles θ_x and θ_y that rotate a vector parallel to the z-axis of the lab reference frame to the vector normal to the plane of the triangle

$$A = \frac{1}{2} \|\underline{E}_1 \times \underline{E}_2\|, \quad \theta_x = -\arctan(N_y, N_z), \quad \theta_y = \arctan(N_x, 1 - N_x^2). \quad (3)$$

Here, $\arctan(x, y)$ is the element wised arc tangent of x/y , and N_i is a component of the unit vector normal to the triangle plane.

For each triangle, we define the triangle shape tensor $\underline{\underline{S}}^{3d}$ as a tensor that maps a reference equilateral triangle with area A_0 lying in the xy-plane, defined by the vectors vectors \underline{C}_i to the current triangle

$$\underline{E}_i = \underline{\underline{S}}^{3d} \underline{C}_i. \quad (4)$$

The vectors of the reference equilateral triangle are

$$\underline{C}_1 = \begin{pmatrix} l \\ 0 \\ 0 \end{pmatrix}, \quad \underline{C}_2 = \begin{pmatrix} l/2 \\ \sqrt{3}/2l \\ 0 \end{pmatrix}, \quad \underline{C}_3 = \begin{pmatrix} 0 \\ 0 \\ 1 \end{pmatrix}, \quad (5)$$

where the side length $l = \sqrt{4A_0/\sqrt{3}}$ with $A_0 = 1$.

The triangle shape tensor $\underline{\underline{S}}^{3d}$ can be written in terms of a planar state tensor $\underline{\underline{S}}^{planar}$ in the reference frame of the triangle as

$$\underline{\underline{S}}^{3d} = \underline{\underline{R}}_x(\theta_x) \underline{\underline{R}}_y(\theta_y) \underline{\underline{S}}^{planar}, \quad (6)$$

where $\underline{\underline{R}}_x(\theta_x)$ and $\underline{\underline{R}}_y(\theta_y)$ are rotations around the x and y axis, respectively. The angles θ_x and θ_y are defined in Eq. 3. The planar triangle state tensor, represented by a 3x3 matrix with the z components set to 0, can be decomposed

535 as

$$\underline{\underline{S}}^{\text{planar}} = \sqrt{\frac{A}{A_0}} \underline{\underline{R}}_z(\phi) \exp(\|\underline{\underline{\tilde{Q}}}\| \underline{\gamma}) \underline{\underline{R}}_z(-\phi) \underline{\underline{R}}_z(\theta_z) \quad (7)$$

536 as in TissueMiner. Here, $\underline{\gamma}$ is a diagonal matrix with diagonal elements
 537 $\{1, -1, 0\}$, and $\underline{\underline{R}}_z$ is the rotation matrix around the z-axis. A is the area of
 538 the triangle, $\|\underline{\underline{\tilde{Q}}}\|$ the magnitude of the elongation tensor, ϕ the direction of
 539 elongation in the xy-plane, and θ_z is the rotation angle around the z-axis relative
 540 to the reference unilateral triangle. The 3D elongation tensor $\underline{\underline{\tilde{Q}}}$ in the
 541 lab reference frame and the elongation tensor in the xy-plane of the triangle
 542 $\underline{\underline{\tilde{Q}}}^{\text{planar}}$ are related by

$$\underline{\underline{\tilde{Q}}} = \underline{\underline{R}}_x(\theta_x) \underline{\underline{R}}_y(\theta_y) \underline{\underline{\tilde{Q}}}^{\text{planar}} \underline{\underline{R}}_x(-\theta_y) \underline{\underline{R}}_y(-\theta_x) \quad (8)$$

543

$$\underline{\underline{\tilde{Q}}}^{\text{planar}} = \underline{\underline{R}}_z(\phi) \exp(\|\underline{\underline{\tilde{Q}}}\| \underline{\gamma}) \underline{\underline{R}}_z(-\phi). \quad (9)$$

544 The magnitude of elongation is calculated as [49]

$$\|\underline{\underline{\tilde{Q}}}\| = \operatorname{arcsinh} \left(\frac{\|\underline{\underline{S}}^{ts}\|}{\sqrt{\|\underline{\underline{S}}^{ta}\|^2 - \|\underline{\underline{S}}^{ts}\|^2}} \right). \quad (10)$$

545 where $\|\underline{\underline{S}}^{ta}\|$ and $\|\underline{\underline{S}}^{ts}\|$ are the norms of the trace-antisymmetric and traceless-
 546 symmetric part of the planar triangle state tensor $\underline{\underline{S}}^{\text{planar}}$, respectively. The
 547 angle of the elongation tensor is given by

$$\phi = \frac{1}{2} \operatorname{arctan2}(B_{xy}, B_{xx}), \quad (11)$$

548 where B_{ij} are the components of the nematic part of the triangle state tensor
 549 $\underline{\underline{S}}$ and $\operatorname{arctan2}(x1, x2)$ the inverse tangent of $x1/x2$, where the sign of $x1$ and
 550 $x2$ is taken into account. In this way, one can select the branch the multivalued
 551 inverse tangent function that corresponds to the angle defined by the point
 552 $(x1, x2)$ in a plane.

553 We now define the cell elongation tensor as the area-weighted average of
 554 the corresponding triangle elongations

$$\underline{\underline{Q}}^\alpha = \frac{1}{A^\alpha} \sum_{t \in \text{cell}} a^t \underline{\underline{Q}}^t, \quad (12)$$

555 where A^α is the area of the cell, a^t the area of a triangle that overlaps with
 556 the cell, and $\underline{\underline{Q}}^t$ is the elongation tensor of that triangle.

557 To calculate the radial component of the cell elongation tensor relative to
 558 the origin in cell α , we first define the radial direction. To this end, we use a 3D
 559 vector \underline{r} connecting the origin to the cell centroid and we project its direction
 560 $\hat{\underline{r}} = \underline{r}/\|\underline{r}\|$ into the tangent plane of the cell, which defines the in-plane radial

direction \hat{r}_{tangent} . The tangent plane of the cell is defined by its normal vector 561
 \hat{N} defined in Eq. 1. We calculate the radial components of the cell elongation 562
tensor as 563

$$Q_{rr} \equiv \hat{r}_{\text{tangent}} \cdot \underline{\underline{Q}} \cdot \hat{r}_{\text{tangent}} \quad (13)$$

relative to the origin. 564

In the DVB, multiple cells form the origin. To calculate $Q_{\rho\rho}$, the vector $\underline{\rho}$ 565
connects the cell centroid to the averaged position of the topologically nearest 566
cells of $k = 0$. We project its direction $\hat{\rho} = \underline{\rho}/\|\underline{\rho}\|$ into the tangent plane of 567
the cell α , which defines the in-plane direction $\hat{\rho}_{\text{tangent}}$ from DVB origin. We 568
calculate the components of the cell elongation tensor as 569

$$Q_{\rho\rho} \equiv \hat{\rho}_{\text{tangent}} \cdot \underline{\underline{Q}} \cdot \hat{\rho}_{\text{tangent}}. \quad (14)$$

7.7 Topological distance coordinate system

570

To calculate topological distances between any two cells, we determine the 571
topological network using the python-igraph library [50]. 572

In each of the tissue regions, we define separate origins: 573

- outDVB region: To define the origin of the outDVB regions, we first determine 574
the pouch margin cells as cells that live on the outermost row of the 575
segmentation mask and do not overlap with the DVB ROI. Then, for each 576
cell in the region, we calculate the shortest topological distance to the margin 577
cells. This identifies the set of maximally distant cells that have the maximal 578
shortest topological distance to the margin. The origin is then defined as 579
the cell that is neighboring the DVB and is at the shortest metric distance 580
to the averaged position of maximally distant cells. At larval stages, both 581
dorsal and ventral sides of the outDVB region are visible, and an origin cell 582
is defined on both sides. 583
- DVB region: We define the origin to consist of a line of cells transversing 584
the DVB. At larval stages, the origin cells are defined as those cells within 585
 $\sqrt{A_{\text{cell}}/\pi} * 1.2$ distance to a straight line connecting the dorsal and ventral 586
center cells. For pupal stages, the origin cells for the DVB are defined as the 587
first row of cells next to the margin of the segmentation mask on the distal 588
side. 589

The so-identified origin cells serve as the origin for the topological distance (k) 590
for each cell in the tissue. In this way, k follows the radial direction along the 591
surface for the outDVB and the path along the the DVB for the DVB. 592

3D visualization of cell properties: We visualize cellular properties and 593
cell elongation tensors on the 3D segmentation mask using paraview [43]. 594

To plot a rank 2 tensor, like the cell elongation tensor, we take the largest 595
eigenvalue of $\underline{\underline{Q}}^\alpha$ as the norm of elongation and the corresponding eigenvector 596
as the direction of elongation that we can plot to the surface. Note that for 597

598 cells / patches that are reasonably flat, the eigenvector with the eigenvalue
 599 closest to zero is (almost) parallel to the normal vector on the patch.

600 **Spatial analysis of cell properties:** We acquired data for 5 to 7 wing discs
 601 of each developmental stage. Images that were not of segment-able quality were
 602 excluded from the analysis. We average cell properties by k between dorsal
 603 and ventral for the outDVB and between images from both sides of the DVB.
 604 We use a cell area-weighted average for elongation.

605 7.8 Mechanics of the programmable spring lattice

606 We use a programmable spring lattice in the shape of a spherical cap to model
 607 the wing disc pouch, which is an epithelial monolayer.

608 **Approximating the wing disc pouch as a spherical cap:** We calculate
 609 the average radius of curvature of the apical side of the wing disc pouch at
 610 wL3 stage in the topologically tracked region as $R = 77.66\mu m$. The angular
 611 size of the spherical cap, denoted by θ_M , is given by

$$\theta_M = \frac{1}{2} \left(\frac{w_{DV} + 2w_{ODV}}{R} \right), \quad (15)$$

612 where w_{DV} is the width of the DVB and w_{ODV} is the average in-surface dis-
 613 tance from the DVB to the periphery of the outDVB region (Extended Data
 614 Fig. S8a). We calculate $w_{DV} = 15\mu m$ and $w_{ODV} = 59.77\mu m$. Using these cal-
 615 culated dimensions, we determine $\theta_M = 49.63^\circ$.

616 **Generating the lattice :** We first generate a triangular lattice in the shape
 617 of a hollow sphere, keeping the radius of curvature R calculated above. This
 618 lattice was obtained using the function *meshzoo.icosa_sphere* available in the
 619 Python package Meshzoo (www.github.com/meshpro/meshzoo). In this func-
 620 tion, we set the argument *refine_factor* = 30, which leads to edges of length
 621 $3.11 \pm 0.18\mu m$. This edge length was found to be small enough to prevent
 622 computational errors in the simulations of this study. We then cropped the
 623 spherical lattice to obtain a spherical cap of angular size θ_M (calculated above,
 624 Extended Data Fig. S8b). Next, we place a second layer at the bottom of this
 625 lattice at a separation of h . This new layer is identical to the original lattice
 626 in terms of the topology of the lattice network but is rescaled to have a radius
 627 of curvature of $R - h$. We connect the two layers with programmable springs
 628 using the topology shown in the inset of Extended Data Fig. S8c. The lattice
 629 obtained this way represents an elastic surface of thickness h , which can be
 630 changed to tune the bending rigidity of the model. Vertices typically have 13
 631 neighbors (6 on their own layer and 7 on the other layer). However, six to eight
 632 vertices out of about 3220 vertices in the whole network form point defects.
 633 These vertices have 11 neighbors.

634 In order to remove any possible effects coming from the lattice structure
 635 (angle of edges or degree of connectivity), we perform simulations for each
 636 condition by taking spherical caps from 50 different regions of the sphere and
 637 averaging the result. We see only very small variability in the final shape,

quantified by the standard deviation of the curvature change profiles in our 638
model results. Thus, we conclude that the lattice structure does not affect our 639
results. 640

Elastic energy of model: The edges of the lattice act as overdamped elastic 641
springs with rest lengths equal to their initial lengths. Hence the model is 642
stress-free at $T = 0$ 643

$$\delta_T^a = \|\Delta\underline{X}^a\| \quad (16)$$

where a denotes a single spring; $\Delta\underline{X}^a$ denotes the spring vector given by $\underline{X}^\beta - 644$
 \underline{X}^α , where α and β are the vertices at the two ends of spring a and \underline{X}^α denotes 645
the position vector of vertex α . During a consequent time step T , the rest 646
length of spring a (δ_T^a) can differ from its current length δ . The elastic energy 647
of this state for the whole lattice is given by 648

$$W = \frac{1}{2} \sum_a k(\delta^a - \delta_T^a)^2, \quad (17)$$

where the sum is over all springs of the network and k represents the spring 649
constant. At each computational time step T , the model tries to find a preferred 650
configuration by minimizing W , hence T acts as a “quasi-static time step”. To 651
minimize the energy of the model at a given T , we use overdamped dynamics 652
with smaller time steps τ , which restart for each new quasi-static time step T . 653

$$\begin{aligned} \frac{d\underline{x}^\alpha}{d\tau} &= -\frac{1}{\gamma} \frac{\partial W}{\partial \underline{x}^\alpha} \\ &= -\frac{k}{\gamma} \sum_a (\delta^a - \delta_T^a) \hat{\underline{\delta}}^a. \end{aligned} \quad (18)$$

Here, γ represents the friction coefficient. \underline{x}^α corresponds to the current posi- 654
tion of the vertex α . δ^a is the length of the springs connected to vertex α . 655
 $\hat{\underline{\delta}}^a = (\underline{x}^\alpha - \underline{x}^\beta)/\delta^a = (\Delta\underline{X}^a)/\delta^a$ represents the unit vector along the spring a 656
that connects vertices α and β . 657

We relax the model at each quasi-static time step T to achieve force balance 658
by updating the positions of the particles using 659

$$\underline{x}^\alpha(\tau + d\tau) = \underline{x}^\alpha(\tau) - d\tau \frac{k}{\gamma} \sum_a (\delta^a - \delta_T^a) \hat{\underline{\delta}}^a, \quad (19)$$

where $d\tau \frac{k}{\gamma}$ was set to 0.01 (ensuring no numerical artifacts). 660

The particles were moved until the average movement of the particles 661
 $(\|\underline{x}^\alpha(\tau + d\tau) - \underline{x}^\alpha(\tau)\|)/R$ reduced to 10^{-9} , where R is the radius of curvature 662
of the outer surface of the spherical cap in the initial stress-free state. 663

7.9 Spontaneous strain tensor 664

Tissue shape change during development is modelled in this work as the 665
appearance of spontaneous strains, a change in the ground state of local length 666

26 *The evertng Drosophila wing disc is a shape-programmed material*

667 scales. This notion can be captured with a spontaneous strain tensor field,
 668 $\underline{\lambda}(\underline{X})$, a rank 2 tensor. Each component corresponds to the multiplicative fac-
 669 tor by which the rest lengths of the material changes in a particular direction.
 670 In some general coordinate system, we can write $\underline{\lambda}$ as

$$\underline{\lambda} = \begin{pmatrix} \lambda_{11} & \lambda_{12} & \lambda_{13} \\ \lambda_{21} & \lambda_{22} & \lambda_{23} \\ \lambda_{31} & \lambda_{32} & \lambda_{33} \end{pmatrix}. \quad (20)$$

671 We choose the coordinate system so that it aligns with our desired deformation
 672 pattern. In this case, $\underline{\lambda}(\underline{X})$ is in a diagonal representation :

$$\underline{\lambda} = \lambda_{11}(\underline{e}_1 \otimes \underline{e}_1) + \lambda_{22}(\underline{e}_2 \otimes \underline{e}_2) + \lambda_{33}(\underline{e}_3 \otimes \underline{e}_3), \quad (21)$$

673 where the basis vectors are chosen such that $\underline{e}_1, \underline{e}_2$ are surface tangents while
 674 \underline{e}_3 is surface normal. In general, we keep $\lambda_{33} = 1$, since we do not input any
 675 spontaneous strains along the thickness of the model.

676 The surface components of $\underline{\lambda}$ can be further broken down into isotropic
 677 and anisotropic components. Isotropic deformation changes the local area of
 678 the surface by changing the local lengths equally in all directions. Anisotropic
 679 deformation increases the local length in one direction while decreasing the
 680 local length in the other direction so as to preserve the local area. Thus,
 681 we decompose the deformation as a product of isotropic and anisotropic
 682 contributions.

$$\begin{aligned} \lambda_{11} &= \lambda \tilde{\lambda} \\ \lambda_{22} &= \lambda \tilde{\lambda}^{-1}. \end{aligned} \quad (22)$$

683 Then, the spontaneous deformation tensor can be written as

$$\underline{\lambda} = \lambda \tilde{\lambda} (\underline{e}_1 \otimes \underline{e}_1) + \lambda \tilde{\lambda}^{-1} (\underline{e}_2 \otimes \underline{e}_2) + (\underline{e}_3 \otimes \underline{e}_3). \quad (23)$$

684 Finally, as $\underline{\lambda}$ is a field, each of the components in the above equation generally
 685 depend on the location on the surface, \underline{X} .
 686 **Discretizing $\underline{\lambda}$:** As our spring lattice is discrete in nature, we use the following
 687 strategy to discretize $\underline{\lambda}$. For a single spring, $\underline{\lambda}$ is an average of the value of $\underline{\lambda}$
 688 on the two ends of the springs.

$$\underline{\lambda}^a = \frac{1}{2} \left(\underline{\lambda}(\underline{X}^\alpha) + \underline{\lambda}(\underline{X}^\beta) \right), \quad (24)$$

689 where α and β are the two vertices of the spring a .

690 **Assigning new rest lengths to springs:** The initial length of spring a
 691 connecting vertices α and β is given by

$$\delta_I^a = \|\underline{X}^\alpha - \underline{X}^\beta\| = \|\Delta \underline{X}^a\|. \quad (25)$$

To assign new rest lengths, we use

692

$$\delta_F^a = \|\underline{\lambda}^a \cdot \Delta \underline{X}^a\|. \quad (26)$$

Note that we assign a new rest length to any spring a based on the positions of its vertices (\underline{X}^α and \underline{X}^β), independent of the layer in which these vertices lie (top and bottom).

Implementing shape change over time: We increase the spontaneous strain slowly to model the slow build up of stresses due to cell behaviours. Hence, we first calculate the target rest length of springs (δ_T^a). At each time step, we assign a rest length δ_I^a and minimize the energy of the model. We increase δ_I^a in a simple linear manner from δ_I^a to δ_F^a

$$\delta_T^a = \delta_I^a + (\delta_F^a - \delta_I^a) \frac{T}{T_F}, \quad (27)$$

where T_F is the number of quasi-static time steps in which the whole simulation takes place. Note that within each time step, the lattice is brought to a force balance state. The simulations were performed for different choices of T_F (1, 2, 5), but we found that the differences in output shapes were undetectable. Still, $T_F = 5$ was chosen to simulate the slow appearance of spontaneous strains.

Measuring resulting strains in model: In our spring model, displacements are defined by positions of vertices and we define the deformation gradient tensor $\underline{\underline{F}}^\alpha$ at each vertex α of the network.

For each spring a emerging from the vertex α , the deformation gradient tensor should satisfy

$$\underline{x}^a = \underline{\underline{F}}^\alpha \underline{X}^a. \quad (28)$$

However, $\underline{\underline{F}}^\alpha$ contains 9 degrees of freedom, while there are 13 springs for each vertex and therefore 13 independent equations to be satisfied. Note that six to eight vertices out of about 3220 vertices in the whole network form point defects and thus have 11 springs. Therefore, we define $\underline{\underline{F}}^\alpha$ as the tensor that best satisfies conditions in Eqs. 28 by minimizing the sum of residuals squared

$$S = \sum_a \|\underline{\underline{F}}^\alpha \underline{X}^a - \underline{x}^a\|^2. \quad (29)$$

This is an ordinary least squares (OLS) problem split into three independent basis vectors. We solved this OLS using the Numpy method `numpy.linalg.lstsq` in cartesian coordinates [51]. We then express $\underline{\underline{F}}$ in the coordinate system corresponding to vertex α in the model explained above. From this, we calculate the isotropic (F) and anisotropic (\tilde{F}) components using

$$F = \sqrt{F_{rr} F_{\phi\phi}} \quad (30)$$

$$\tilde{F} = \sqrt{F_{rr}/F_{\phi\phi}}. \quad (31)$$

721 Finally, we compute $\underline{\underline{\lambda}}^{\text{res}}$ as

$$\underline{\underline{\lambda}}^{\text{res}} = \underline{\underline{F}} \underline{\underline{\lambda}}^{-1}. \quad (32)$$

722 The isotropic (λ^{res}) and anisotropic components ($\tilde{\lambda}^{\text{res}}$) of $\underline{\underline{\lambda}}^{\text{res}}$ are calculated
723 in the same way as for $\underline{\underline{F}}$.

724 7.10 Nematic director pattern on spherical surface

725 In the initial state of the model, we specify a coordinate system on the spherical
726 surface in different regions (outDVB and DVB). These coordinate systems are
727 chosen such that the observed nematic patterns of spontaneous strains ($\hat{\lambda}$)
728 align with the major axes of the chosen coordinate systems.

729 We first define the origins in our model similar to the origins defined in
730 the data. To do so, we first measure θ_{DV} (Extended Data Fig. 12 a). The
731 coordinates of O_D and O_V are then given by $(\pm R \sin(\theta_{DV}/2), 0, R \cos(\theta_{DV}/2))$
732 in the cartesian coordinate system. The center for the DVB region is given by
733 the line O_{DV} which joins O_D and O_V .

734 In the outDVB region, we have a coordinate system in which the basis vec-
735 tors are given by $\underline{e}_r, \underline{e}_\phi, \underline{e}_h$ (Extended Data Fig. S8). \underline{e}_h is simply the normal
736 vector on the spherical surface. To calculate \underline{e}_r at a point, we draw a vector
737 from the origin in this region (O_D or O_V) to the point. We then take a pro-
738 jection of this vector onto the tangent plane of the surface and normalize it to
739 give us a unit vector. In this way, we calculate \underline{e}_r as a surface tangent vector
740 emanating radially outwards from the origins of the outDVB regions. \underline{e}_ϕ is then
741 the direction perpendicular to \underline{e}_r and \underline{e}_h . For each point in the outDVB region,
742 we calculate the geodesic distance between the point and the center point of
743 its region. We then normalize this distance by the maximum geodesic distance
744 from the center calculated in this region. This gives us a scalar coordinate r
745 which varies from 0 to 1.

746 In the DVB region, the basis vectors are given by $(\underline{e}_\rho, \underline{e}_w, \underline{e}_h)$ (Extended
747 Data Fig. S8). \underline{e}_h is simply the normal vector on the spherical surface. To
748 calculate \underline{e}_ρ at a point, we draw a vector from the nearest point on O_{DV} to
749 the point. We then take a projection of this vector onto the tangent plane of
750 the surface and normalize it to give us a unit vector. In this way, we calculate
751 \underline{e}_ρ as a surface tangent vector emanating outwards from the center line of the
752 DVB region as well as parallel to the DVB. \underline{e}_w is perpendicular to \underline{e}_ρ and
753 \underline{e}_h . For each point in the outDVB region, we calculate the shortest distance
754 between the point and the center line of the DVB region. We then normalize
755 this distance by the maximum distance from the center line in the DVB region.
756 This gives us a scalar coordinate ρ .

757 For the simple examples presented in Fig 2c (except Fig 2c.iii), θ_{DV} was
758 set to be 0 to have a simple radial coordinate system. For Fig 2c.iii, $\theta_{DV} > \theta_M$.

7.11 Extracting the strain pattern from segmented images

To quantify the strain due to different cell behaviors along the basis vectors of the chosen coordinate system, we compare cells within topologically tracked bins between two different developmental stages.

Tracking location between developmental stages: We leverage the topological distance coordinate system to track locations between discs. Each topological ring k is given a value N which denotes the cumulative number of cells from the topological origin defined in each region (O_D , O_V , and O_{DV}). We use N to track the location in our static images of different discs at different developmental stages.

Observed strain due to cell area change: Cell area scales with square of the distance between cell vertices. Thus, the factor by which the local lengths change in all directions is given by

$$\lambda_A^*(N) = \sqrt{\frac{A(N, t + \Delta t)}{A(N, t)}}. \quad (33)$$

Here, t corresponds to an initial developmental stage, and $t + \Delta t$ corresponds to a later developmental stage. A refers to the average cell area evaluated at N .

Observed strain due to cell elongation change: Each cell is given a cell elongation tensor $\underline{\underline{Q}}$ that is the average of further subdivisions of the cell polygon into triangles (Methods 7.6). Each triangle can be circumscribed by an ellipse, the centroid of which coincides with the centroid of the triangle. According to [52], the length of the long axis of the ellipse is given by $l = r_o \exp(\|\underline{\underline{Q}}\|)$, where r_o is the radius of a reference equilateral triangle. The length of the short axis of the ellipse is given by $s = r_o \exp(-\|\underline{\underline{Q}}\|)$. The axes of the ellipse match with the radial and tangential directions if the off-diagonal components $Q_{r\phi}$ or $Q_{\rho\phi}$ are approximately 0. This was the case for our data as well. The length scale associated with the radial direction is l if Q_{rr} or $Q_{\rho\rho}$ is positive and s if Q_{rr} or $Q_{\rho\rho}$ is negative. Thus, we get a measure of the length scales along the radial direction, which we denote by L and is given by

$$L = \exp(\sigma \|\underline{\underline{Q}}\|), \quad (34)$$

where σ is the sign of Q_{rr} or $Q_{\rho\rho}$.

We then average L within each ring and compute a ratio of the length scales along the radial direction between two developmental stages by computing

$$\tilde{\lambda}_Q^*(N) = \frac{L(N, t + \Delta t)}{L(N, t)}. \quad (35)$$

Observed strain due to cell rearrangements: Rearrangements lead to

792 anisotropic deformation of the tissue. In our topological coordinate system,
 793 radially oriented rearrangements lead to an increase in the number of rings
 794 needed to accommodate some fixed number of cells (Extended Data Fig. S6).
 795 Similarly, tangential rearrangements would lead to a decrease in the number of
 796 topological rings. Thus, by measuring the change in the number of rings needed
 797 to accommodate some fixed number of cells, we can estimate the deformation
 798 due to the net effect of radial and tangential rearrangements.

799 In a tissue region at developmental stage t , let us consider a single ring with
 800 index k and cumulative number of cells N . Ring k contains ΔN cells given by
 801 $N(k, t) - N(k - 1, t)$. By construction, the number of rings needed to contain
 802 ΔN cells at location N is given by $n(N, t) = 1$. For a later developmental stage,
 803 $t + \Delta t$, we estimate $n(N, t + \Delta t)$ which is the number of rings that contain
 804 ΔN cells at the location N . This is done by taking the difference between k
 805 values evaluated at $t + \Delta t$ and at locations $N(k - 1, t)$ and $N(k, t)$ (see also
 806 Extended Data Fig. S6)

$$n(N, t + \Delta t) = k(N(k, t), t + \Delta t) - k(N(k - 1, t), t + \Delta t) \quad (36)$$

807 As $n(N, t)$ and $n(N, t + \Delta t)$ are measures of the number of topological rings,
 808 they represent the radial topological length scales that change due to cell
 809 rearrangements. Thus, the strain due to cell rearrangements is quantified by

$$\lambda_R^*(N) = \frac{n(N, t + \Delta t)}{n(N, t)}. \quad (37)$$

810 $\lambda_R^*(N) > 1$ represents radial extension of the tissue due to radially oriented
 811 rearrangements, while $\lambda_R^*(N) < 1$ represents tangential extension.

812 **Observed strain due to combination of cell elongation change and**
 813 **cell rearrangements:** The combined strain due to cell elongation change and
 814 cell rearrangements is given by

$$\tilde{\lambda}^*(N) = \tilde{\lambda}_Q^*(N)\tilde{\lambda}_R^*(N). \quad (38)$$

815
 816 **Mapping locations between wing disc images and model:** In the model,
 817 we have a dimensionless scalar coordinate in the outDVB and DVB regions
 818 varying from 0 to 1. In the data as well, we prescribe a scalar coordinate to
 819 each topological bin. To do so, we calculate the path length in μm of the
 820 shortest path along cell centers from each cell to the origin and average this
 821 path length for each topological bin. For each bin, we normalize this path
 822 length by the average path length of the outermost topological bin in the
 823 corresponding region (DVB or outDVB). We call this normalized path length
 824 r for the outDVB region and ρ for the DVB region. Due to our normalization,
 825 r and ρ run from 0 to 1, similar to the model.

826 Thus, we are able to map any topological ring (identified by k and N) to
 827 a scalar coordinate r in outDVB or ρ in DVB. In Methods 7.10, we explain

the mapping between r and ρ to the cartesian coordinates of the vertices in
828 the model given by \underline{X}^α , where α is a vertex. Using this mapping, any strain
829 component, for example $\tilde{\lambda}_R^*(\underline{X}^\alpha)$, on the model vertex α can be evaluated from
830 a corresponding $\tilde{\lambda}_R^*(N)$.
831

7.12 Quantifying curvature of cross-sections

Tissue shape analysis is performed on multi-angle fused SPIM images. We used
833 Fiji re-slicing tools to generate two orthogonal cross-sections along the apical-
834 basal direction. Across-DVB is a cross-section along the center of the long axis
835 of the wing disc. To find the center, we used the position of the sensory organ
836 precursors and general morphology. The along-DVB cross-section follows the
837 DVB and was identified by Ecadherin-GFP signal intensity. The apical pouch
838 shape was outlined manually along both directions over the pouch region up to
839 the HP-fold using custom Fiji macros. Subsequent pouch shape analysis was
840 performed in Python. The tissue shape information was extracted form Fiji
841 into Python using the Python ‘read-roi’ package.
842

The extracted apical shapes were aligned and rotated for each wing disc as
843 follows. First, starting from the left-most point in the curve, we measure the
844 arc length of the curve in the clockwise direction. The arc length of the i th
845 point on the curve is given by
846

$$s(i) = \sum_{i=2}^n \|\underline{x}_i - \underline{x}_{i-1}\|, \quad (39)$$

where n is the number of points in the discrete curve and $\underline{x}_i = (x_i, y_i)$ is the
847 position vector of the i th point. We keep $s(i=1) = 0$.
848

Next, we define the center of the curve at the middle and offset the arc
849 lengths to have $s = 0$ at the center. This leads to negative arc lengths on the
850 left side of the center and positive arc lengths on the right side of the center
851 (Extended Data Fig. S1).
852

In order to compute a mean curve from different wing discs of the same
853 developmental stage, we translate and rotate the curves (Extended Data Fig.
854 S1b). We translate each curve by setting their midpoints as the origin $(0, 0)$. To
855 rotate the curve, we compute the center of mass of the curve. Then, we define
856 the new y axis as the line that joins the center of mass to the origin. Finally,
857 for each curve, we smoothen and interpolate between the discrete points using
858 spline interpolation. We use the `scipy.interpolate.UnivariateSpline` function of
859 `scipy` [53]. To smoothen the spline, we define five knot points, one being the
860 mid-point of the curve, and two others being at three-fourth and half of length
861 from mid-point from either sides. Next, we compute the curvature of each
862 curve using the following expression
863

$$\kappa = \frac{x'y'' - y'x''}{(x'^2 + y'^2)^{\frac{3}{2}}}, \quad (40)$$

32 *The evertng Drosophila wing disc is a shape-programmed material*

864 where ' refers to the derivative with respect to the parameter of the curve,
 865 which is arc length in our case.

866 Finally, to compute an average curve, we get the average position vectors at
 867 arc lengths starting from a minimum arc length until a maximum arc length in
 868 intervals of $5\mu m$. We do similar averaging for curvature values to get average
 869 curvature profiles.

870 To calculate the change in curvature, we normalize each curve from 0 to
 871 1 and use a linear interpolation with 40 positions to subtract the initial from
 872 subsequent curvatures. We then re-introduce the average arc length for each
 873 each developmental stage for each of the normalized positions.

874 **Model output:** To quantify the curvature of the model output, we first isolate
 875 the top layer of the lattice. Then, we take the along-DVB cross-section (XZ
 876 plane) and the across-DVB cross-section (YZ plane). To take the cross-section,
 877 we record the points of intersection of the in-surface springs with the respective
 878 plane of the cross-section. From this, we get a discrete set of points that are
 879 ordered along their horizontal position to get a counter-clockwise curve. This
 880 curve data is now similar to the data we obtain from segmented images. Hence,
 881 we apply the exact same procedure describe above to quantify the curvature
 882 of the model output.

883

7.13 Tuning thickness

884 We tune the thickness of the model in order to change the bending modulus. We
 885 first perform simulations by inputting all cell behaviours (cell area changes, cell
 886 elongation changes and cell rearrangements) combined as spontaneous strains.
 887 We perform this simulation for different thicknesses $h/R = 0.05, 0.1, 0.15$,
 888 where h is the thickness of the model and R is the radius of curvature of the
 889 top surface of the initial state of the model (Extended Data Fig. S9a). We find
 890 that $h/R = 0.1$ gives us the best matching of the curvature change profiles
 891 with the wing disc pouch. Fixing $h/R = 0.1$, we perform further analysis to
 892 infer the spontaneous strains in the wing disc pouch. Inputting these inferred
 893 spontaneous strains, we again performed simulations for different thicknesses.
 894 We found $h/R = 0.1$ still matchs the wing disc pouch curvature change values
 895 best (Extended Data Fig. S9b).

896

Acknowledgements

897 We thank Christian Dahmann, Anne Classen, and past/present members of the
 898 Eaton, Dye, Modes, Julicher, and Popovic teams for discussions on the project
 899 prior to publication. Miki Ebisuya gave thoughtful feedback on the manuscript.
 900 We also thank the Light Microscopy Facility, the Computer Department, and
 901 the Fly Keepers of the MPI-CBG, as well as the Bioimage Analysis group
 902 at PoL for their support and expertise. This work was funded by Germany's
 903 Excellence Strategy – EXC-2068 – 390729961– Cluster of Excellence Physics
 904 of Life of TU Dresden, as well as grants awarded to SE from the Deutsche

Forschungsgemeinschaft (SPP1782, EA4/10-2) and core funding of the Max- 905
Planck Society. NAD additionally acknowledges funding from the Deutsche 906
Krebshilfe (MSNZ P2 Dresden). AK was funded through the Elbe PhD pro- 907
gram. CD acknowledges the support of a postdoctoral fellowship from the 908
LabEx “Who Am I?” (ANR-11-LABX-0071) and the Université Paris Cité 909
IdEx (ANR-18-IDEX-0001) funded by the French Government through its 910
“Investments for the Future”. We dedicate this work to our coauthor Prof. Dr. 911
Suzanne Eaton, who tragically passed away near the beginning of the project. 912

Author Contributions

JFF: Conceptualization, Methodology, Software, Validation, Formal analysis, 914
Investigation, Data Curation, Writing - Original Draft, Visualization 915
AK: Conceptualization, Methodology, Software, Validation, Formal analysis, 916
Investigation, Data Curation, Writing - Original Draft, Visualization 917
JP: Methodology, Software, Validation, Data Curation 918
CD: Methodology, Validation 919
SE: Conceptualization, Resources, Funding acquisition, Supervision 920
MP: Methodology, Validation, Writing - Original Draft 921
FJ: Conceptualization, Writing - Original Draft, Supervision 922
CDM: Conceptualization, Methodology, Resources, Writing - Original Draft, 923
Project administration, Supervision, Funding acquisition 924
NAD: Conceptualization, Methodology, Resources, Writing - Original Draft, 925
Project administration, Supervision, Funding acquisition 926

References

- [1] Miriam Osterfield, Xinxin Du, Trudi SchÃ¶pbach, Eric Wieschaus, and Stanislav Y. Shvartsman. Three-dimensional epithelial morphogenesis in the developing Drosophila egg. *Dev Cell*, 24(4):400–410, February 2013. 928
929
930
 - [2] Noah P Mitchell, Dillon J Cislo, Suraj Shankar, Yuzheng Lin, Boris I Shraiman, and Sebastian J Streichan. Visceral organ morphogenesis via calcium-patterned muscle constrictions. *eLife*, 11, May 2022. 931
932
933
 - [3] Amy E. Shyer, Tuomas Tallinen, Nandan L. Nerurkar, Zhiyan Wei, Eun Seok Gil, David L. Kaplan, Clifford J. Tabin, and L. Mahadevan. Villification: How the gut gets its villi. *Science*, 342(6155):212–218, October 2013. 934
935
936
937
 - [4] David Bilder and Saori L. Haigo. Expanding the morphogenetic repertoire: Perspectives from the drosophila egg. *Developmental Cell*, 22(1):12–23, January 2012. 938
939
940
 - [5] Akankshi Munjal, Edouard Hannezo, Tony Y.-C. Tsai, Timothy J. Mitchison, and Sean G. Megason. Extracellular hyaluronate pressure shaped by 941
942

34 *The evertng Drosophila wing disc is a shape-programmed material*

- 943 cellular tethers drives tissue morphogenesis. *Cell*, 184(26):6313–6325.e18,
944 December 2021.
- 945 [6] Adam C Martin. The physical mechanisms of *Drosophila* gastrulation:
946 Mesoderm and endoderm invagination. *Genetics*, 214(3):543–560, March
947 2020.
- 948 [7] Liyuan Sui, Silvanus Alt, Martin Weigert, Natalie Dye, Suzanne Eaton,
949 Florian Jug, Eugene W. Myers, Frank Jülicher, Guillaume Salbreux, and
950 Christian Dahmann. Differential lateral and basal tension drive fold-
951 ing of drosophila wing discs through two distinct mechanisms. *Nature
952 Communications*, 9(1), November 2018.
- 953 [8] Carl Modes and Mark Warner. Shape-programmable materials. *Physics
954 Today*, 69(1):32–38, January 2016. Publisher: American Institute of
955 Physics.
- 956 [9] E. Efrati, E. Sharon, and R. Kupferman. Elastic theory of unconstrained
957 non-euclidean plates. *Journal of the Mechanics and Physics of Solids*,
958 57(4):762–775, 2009.
- 959 [10] Taylor H. Ware, Michael E. McConney, Jeong Jae Wie, Vincent P.
960 Tondiglia, and Timothy J. White. Voxelated liquid crystal elastomers.
961 *Science*, 347(6225):982–984, 2015.
- 962 [11] Julien Dervaux and Martine Ben Amar. Morphogenesis of growing soft
963 tissues. *Phys. Rev. Lett.*, 101:068101, Aug 2008.
- 964 [12] Utpal Nath, Brian C. W. Crawford, Rosemary Carpenter, and Enrico
965 Coen. Genetic control of surface curvature. *Science*, 299(5611):1404–1407,
966 2003.
- 967 [13] James W. Fristrom, W. Robert Logan, and Collin Murphy. The synthetic
968 and minimal culture requirements for evagination of imaginal discs of
969 *Drosophila melanogaster* in vitro. *Developmental Biology*, 33(2):441–456,
970 August 1973.
- 971 [14] L.I. Fessler, M.L. Condic, R.E. Nelson, J.H. Fessler, and J.W.
972 Fristrom. Site-specific cleavage of basement membrane collagen IV during
973 *Drosophila* metamorphosis. *Development*, 117(3):1061–1069, March 1993.
- 974 [15] Maria-del-Carmen Diaz-de-la Loza, Robert P. Ray, Poulami S. Ganguly,
975 Silvanus Alt, John R. Davis, Andreas Hoppe, Nic Tapon, Guillaume Sal-
976 breux, and Barry J. Thompson. Apical and Basal Matrix Remodeling
977 Control Epithelial Morphogenesis. *Developmental Cell*, 46(1):23–39.e5,
978 July 2018.

- [16] Eva Fekete, Dianne Fristrom, Istvan Kiss, and James W. Fristrom. The mechanism of evagination of imaginal discs of *Drosophila melanogaster* : II. Studies on trypsin-accelerated evagination. *Wilhelm Roux's Archives of Developmental Biology*, 178(2):123–138, June 1975. 979 980 981 982
- [17] Silvia Aldaz, Luis M. Escudero, and Matthew Freeman. Dual role of myosin II during *Drosophila* imaginal disc metamorphosis. *Nature Communications*, 4:1761, 2013. 983 984 985
- [18] D. Fristrom and C. Chihara. The mechanism of evagination of imaginal discs of *Drosophila melanogaster*. V. Evagination of disc fragments. *Developmental Biology*, 66(2):564–570, October 1978. 986 987 988
- [19] Dianne Fristrom. The mechanism of evagination of imaginal discs of *Drosophila melanogaster*; III. Evidence for cell rearrangement. *Developmental Biology*, 54(2):163–171, December 1976. 989 990 991
- [20] M L Condic, D Fristrom, and J W Fristrom. Apical cell shape changes during *Drosophila* imaginal leg disc elongation: A novel morphogenetic mechanism. *Development*, 111:23–33, 1991. 992 993 994
- [21] D. K. Fristrom and J. W. Fristrom. The metamorphic development of the adult epidermis. In *The Development of Drosophila Melanogaster*, volume 2, pages 843–897. Cold Spring Harbor Laboratory Press, 1993. 995 996 997
- [22] Job Taylor and Paul N. Adler. Cell Rearrangement and Cell Division during the Tissue Level Morphogenesis of Evaginating *Drosophila* Imaginal Discs. *Developmental biology*, 313(2):739–751, January 2008. 998 999 1000
- [23] David Hoerl, Fabio Rojas Rusak, Friedrich Preusser, Paul Tillberg, Nadine Randel, Raghav K. Chhetri, Albert Cardona, Philipp J. Keller, Hartmann Harz, Heinrich Leonhardt, Mathias Treier, and Stephan Preibisch. BigStitcher: Reconstructing high-resolution image datasets of cleared and expanded samples. *Nat Methods*, 16(9):870–874, September 2019. 1001 1002 1003 1004 1005 1006
- [24] C. D. Modes and M. Warner. Blueprinting nematic glass: Systematically constructing and combining active points of curvature for emergent morphology. *Physical Review E*, 84(2), Aug 2011. 1007 1008 1009
- [25] Hillel Aharoni, Eran Sharon, and Raz Kupferman. Geometry of thin nematic elastomer sheets. *Phys. Rev. Lett.*, 113:257801, Dec 2014. 1010 1011
- [26] C. D. Modes, K. Bhattacharya, and M. Warner. Gaussian curvature from flat elastica sheets. *Proceedings of the Royal Society A: Mathematical, Physical and Engineering Sciences*, 467(2128):1121–1140, 2011. 1012 1013 1014

36 *The evertng Drosophila wing disc is a shape-programmed material*

- 1015 [27] Carlos M. Duque and Carl D. Modes. Shape programming in entropic
1016 tissues, 2023.
- 1017 [28] Margrit Schubiger and John Palka. Changing spatial patterns of DNA
1018 replication in the developing wing of *Drosophila*. *Developmental Biology*,
1019 123(1):145–153, September 1987.
- 1020 [29] Dianne Fristrom and James W. Fristrom. The mechanism of evagination
1021 of imaginal discs of *Drosophila melanogaster*: I. General considerations.
1022 *Developmental Biology*, 43(1):1–23, March 1975.
- 1023 [30] Timri Aegerter-Wilmsen, Alister C. Smith, Alix J. Christen, Christof M.
1024 Aegerter, Ernst Hafen, and Konrad Basler. Exploring the effects of
1025 mechanical feedback on epithelial topology. *Development (Cambridge,
1026 England)*, 137(3):499–506, February 2010.
- 1027 [31] Loïc LeGoff, Hervé Rouault, and Thomas Lecuit. A global pattern of
1028 mechanical stress polarizes cell divisions and cell shape in the growing
1029 *Drosophila* wing disc. *Development*, 140(19):4051–4059, October 2013.
- 1030 [32] Yanlan Mao, Alexander L Tournier, Andreas Hoppe, Lennart Kester,
1031 Barry J Thompson, and Nicolas Tapon. Differential proliferation rates
1032 generate patterns of mechanical tension that orient tissue growth. *The
1033 EMBO Journal*, 32(21):2790–2803, October 2013.
- 1034 [33] Natalie A Dye, Marko Popović, K Venkatesan Iyer, Jana F Fuhrmann,
1035 Romina Piscitello-Gómez, Suzanne Eaton, and Frank Jülicher. Self-
1036 organized patterning of cell morphology via mechanosensitive feedback.
1037 *eLife*, 10:e57964, March 2021.
- 1038 [34] Peter J. Bryant. Cell lineage relationships in the imaginal wing disc of
1039 *Drosophila melanogaster*. *Developmental Biology*, 22(3):389–411, October
1040 1970.
- 1041 [35] A. Garcia-Bellido, P. Ripoll, and G. Morata. Developmental Compart-
1042 mentalisation of the Wing Disk of *Drosophila*. *Nature New Biology*,
1043 245(147):251–253, October 1973.
- 1044 [36] Natalie A. Dye. Cultivation and Live Imaging of *Drosophila* Imaginal
1045 Discs. *Methods in Molecular Biology (Clifton, N.J.)*, 2540:317–334, 2022.
- 1046 [37] Johannes Schindelin, Ignacio Arganda-Carreras, Erwin Frise, Ver-
1047 ena Kaynig, Mark Longair, Tobias Pietzsch, Stephan Preibisch, Curt-
1048 tis Rueden, Stephan Saalfeld, Benjamin Schmid, Jean-Yves Tinevez,
1049 Daniel James White, Volker Hartenstein, Kevin Eliceiri, Pavel Tomancak,
1050 and Albert Cardona. Fiji: An open-source platform for biological-image
1051 analysis. *Nature Methods*, 9(7):676–682, June 2012.

- [38] Jannis Ahlers, Daniel Althviz Moré, Oren Amsalem, Ashley Anderson, 1052 Grzegorz Bokota, Peter Boone, Jordão Bragantini, Genevieve Buckley, 1053 Alistair Burt, Matthias Bussonnier, Ahmet Can Solak, Clément Capo- 1054 ral, Draga Doncila Pop, Kira Evans, Jeremy Freeman, Lorenzo Gaifas, 1055 Christoph Gohlke, Kabilar Gunalan, Hagai Har-Gil, Mark Harfouche, 1056 Kyle I. S. Harrington, Volker Hilsenstein, Katherine Hutchings, Talley 1057 Lambert, Jessy Lauer, Gregor Lichtner, Ziyang Liu, Lucy Liu, Alan Lowe, 1058 Luca Marconato, Sean Martin, Abigail McGovern, Lukasz Migas, Nada- 1059 lyn Miller, Hector Muñoz, Jan-Hendrik Müller, Christopher Nauroth- 1060 Kreß, Juan Nunez-Iglesias, Constantin Pape, Kim Pevey, Gonzalo Peña- 1061 Castellanos, Andrea Pierré, Jaime Rodríguez-Guerra, David Ross, Loic 1062 Royer, Craig T. Russell, Gabriel Selzer, Paul Smith, Peter Sobolewski, 1063 Konstantin Sofiuk, Nicholas Sofroniew, David Stansby, Andrew Sweet, 1064 Wouter-Michiel Vierdag, Pam Wadhwa, Melissa Weber Mendonça, Jonas 1065 Windhager, Philip Winston, and Kevin Yamauchi. Napari: A multi- 1066 dimensional image viewer for Python, July 2023. 1067
- [39] Robert Haase, Dohyeon Lee, Draga Doncila Pop, and Laura Žigutytė. 1068 Haesleinhuepf/napari-accelerated-pixel-and-object- classification: 0.14.0, 1069 October 2023. 1070
- [40] Robert Haase, Pradeep Rajasekhar, Talley Lambert, grahamross123, Juan 1071 Nunez-Iglesias, Lachie, Clement Caporal, Christophe Avenel, ENicolay, 1072 and Elissavet Sandaltzopoulou. clEsperanto/pyclesperanto-prototype: 1073 0.24.1, April 2023. 1074
- [41] Marco Musy, Guillaume Jacquetot, Giovanni Dalmasso, Jaewook Lee, 1075 Ruben de Bruin, Johannes Soltwedel, Mikael Tull Dahl, Ahinoam Pol- 1076 lack, Brandon Hacha, Federico Claudi, Codacy Badger, Anton Sol, 1077 RobinEnjalbert, Zhi-Qiang Zhou, Andrey Yershov, Bane Sullivan, Brian 1078 Lerner, Daniel Hrisca, Diego Volpatto, Evan, Franco Matzkin, mkerrin- 1079 rapid, Nico Schlömer, RichardScottOZ, Xushan Lu, and Oliver Schneider. 1080 marcomusy/vedo: 2023.4.6, June 2023. 1081
- [42] Robert Haase, Johannes Soltwedel, and Kevin Yamauchi. 1082 Haesleinhuepf/napari-process-points-and-surfaces: 0.5.0, April 2023. 1083
- [43] Charles Law James Ahrens, Berk Geveci. Paraview: An end-user tool for 1084 large-data visualization. In Charles D. Hansen and Chris R. Johnson, 1085 editors, *Visualization Handbook*, pages 717–731. Butterworth-Heinemann, 1086 January 2005. 1087
- [44] Alexander Krull, Tim-Oliver Buchholz, and Florian Jug. Noise2Void - 1088 Learning Denoising from Single Noisy Images, April 2019. 1089
- [45] Natalie A. Dye, Marko Popović, Stephanie Spannl, Raphaël Etournay, 1090 Dagmar Kainmüller, Suhrid Ghosh, Eugene W. Myers, Frank Jülicher, 1091

38 *The evertng Drosophila wing disc is a shape-programmed material*

- 1092 and Suzanne Eaton. Cell dynamics underlying oriented growth of the
 1093 *Drosophila* wing imaginal disc. *Development*, page dev.155069, January
 1094 2017.
- 1095 [46] Benoit Aigouy, Daiki Umetsu, and Suzanne Eaton. Segmentation and
 1096 Quantitative Analysis of Epithelial Tissues. *Methods in Molecular Biology*
 1097 (*Clifton, N.J.*), 1478:227–239, 2016.
- 1098 [47] Raphaël Etournay, Matthias Merkel, Marko Popović, Holger Brandl,
 1099 Natalie A Dye, Benoît Aigouy, Guillaume Salbreux, Suzanne Eaton, and
 1100 Frank Jülicher. *TissueMiner*: A multiscale analysis toolkit to quantify
 1101 how cellular processes create tissue dynamics. *eLife*, 5:e14334, May 2016.
- 1102 [48] Manish Jaiswal, Namita Agrawal, and Pradip Sinha. Fat and Wingless
 1103 signaling oppositely regulate epithelial cell-cell adhesion and distal wing
 1104 development in *Drosophila*. *Development*, 133(5):925–935, March 2006.
- 1105 [49] Matthias Merkel. From cells to tissues: Remodeling and polarity reori-
 1106 entation in epithelial tissues, 2014.
- 1107 [50] Zanini, F., Nepusz, T., Horvát, S., and Traag, V. Igraph/python-igraph,
 1108 January 2015.
- 1109 [51] Charles R. Harris, K. Jarrod Millman, Stéfan J. van der Walt, Ralf
 1110 Gommers, Pauli Virtanen, David Cournapeau, Eric Wieser, Julian Tay-
 1111 lor, Sebastian Berg, Nathaniel J. Smith, Robert Kern, Matti Picus,
 1112 Stephan Hoyer, Marten H. van Kerkwijk, Matthew Brett, Allan Haldane,
 1113 Jaime Fernández del Río, Mark Wiebe, Pearu Peterson, Pierre Gérard-
 1114 Marchant, Kevin Sheppard, Tyler Reddy, Warren Weckesser, Hameer
 1115 Abbasi, Christoph Gohlke, and Travis E. Oliphant. Array programming
 1116 with NumPy. *Nature*, 585(7825):357–362, September 2020.
- 1117 [52] Matthias Merkel, Raphaël Etournay, Marko Popović, Guillaume Salbreux,
 1118 Suzanne Eaton, and Frank Jülicher. Triangles bridge the scales: Quan-
 1119 tifying cellular contributions to tissue deformation. *Physical Review E*,
 1120 95(3):032401, 2017.
- 1121 [53] Pauli Virtanen, Ralf Gommers, Travis E. Oliphant, Matt Haberland,
 1122 Tyler Reddy, David Cournapeau, Evgeni Burovski, Pearu Peterson, War-
 1123 renn Weckesser, Jonathan Bright, Stéfan J. van der Walt, Matthew Brett,
 1124 Joshua Wilson, K. Jarrod Millman, Nikolay Mayorov, Andrew R. J.
 1125 Nelson, Eric Jones, Robert Kern, Eric Larson, C J Carey, İlhan Polat,
 1126 Yu Feng, Eric W. Moore, Jake VanderPlas, Denis Laxalde, Josef Perk-
 1127 told, Robert Cimrman, Ian Henriksen, E. A. Quintero, Charles R. Harris,
 1128 Anne M. Archibald, Antônio H. Ribeiro, Fabian Pedregosa, Paul van Mul-
 1129 bregt, and SciPy 1.0 Contributors. SciPy 1.0: Fundamental Algorithms
 1130 for Scientific Computing in Python. *Nature Methods*, 17:261–272, 2020.